Hydrogen generation during hydrothermal alteration of peralkaline granite

Laurent Truche, Franck Bourdelle, Stefano Salvi, Nicolas Lefeuvre, Apolline Zug, Emily Lloret

Hydrogen generation during hydrothermal alteration of peralkaline granite

Laurent Truche[1]*, Franck Bourdelle[2], Stefano Salvi[3], Nicolas Lefeuvre[1], Apolline Zug[1], Emily Lloret[2]

[1] Université Grenoble Alpes, CNRS, ISTerre, F-38058 Grenoble Cedex 9, France

[2] Univ. Lille, Institut Mines-Télécom, Univ. Artois, Junia, ULR 4515 – LGCgE, Laboratoire de Génie Civil et géo-Environnement, F-59000 Lille, France

[3] Géosciences Environnement Toulouse (GET), CNRS/IRD/UPS/CNES. Toulouse University, 14 avenue Edouard Belin, 31400 Toulouse

* laurent.truche@univ-grenoble-alpes.fr

Abstract

It is well known that oxidation of ferrous to ferric iron by water can generate molecular hydrogen (H_2), with the most widely recognized natural manifestation being serpentinization of olivine and pyroxene in ultramafic rocks. A less known yet extremely important source of natural H_2 are peralkaline igneous intrusions, where spectacular enrichments of H_2 are documented from fluid inclusions and as free gas migrating through fractured rocks and soils. Of these occurrences, the best studied are those at Strange Lake in Canada, Lovozero and Khibiny in Russia, and Ilímaussaq in Greenland. Based on petrographic observations and fluid inclusions analysis, it has been proposed that the hydrothermal alteration of arfvedsonite, an Fe^{II}-bearing amphibole, is the source of H_2 in this context, although it is yet to be unequivocally demonstrated. To investigate the generation of H_2 during alteration of

peralkaline granites, we performed hydrothermal experiments on pure arfvedsonite grains and arfvedsonite-bearing granite (10 wt% arfvedsonite) from the Strange Lake pluton (Canada). These materials, in the presence of aqueous solutions, were sealed inside gold capsules or placed within titanium autoclaves, which allowed monitoring H_2 generation in function of temperature (280–400 °C), chlorinity (0 and 3 m NaCl), pH, and starting mineral assemblage. Blank experiments were conducted to quantify the background amounts of H_2 generated from Au/Ti oxidation, diffusing through the reaction cells, release from fluid inclusions or otherwise occluded in minerals. Solids were characterized by XRD, SEM, TEM on FIB foils, and STXM-XANES. Outcomes of this study demonstrate the production of H_2 in agpaitic peralkaline rocks by the hydrothermal alteration of arfvedsonite. The rate of H_2 production, normalized to the specific surface area of arfvedsonite, increases with temperature from 1100 to 2200 pmol cm^{-2} day^{-1} between 280 and 400 °C, respectively. Chlorinity tends to have a negative impact on the reaction rate, while circumneutral to alkaline conditions clearly promote H_2 generation. Altering whole granite samples instead of arfvedsonite grains only also enhances H_2 production rate. The presence of aluminum, released from microcline and albite dissolution, may increase both the solubility and the dissolution rate of arfvedsonite by promoting precipitation of phyllosilicates. At least two different types of phyllosilicates were observed, chlorite and montmorillonite. Magnetite and secondary zircon were also identified at the surface of reacted arfvedsonite (Zr content = 1200 ppm). The H_2 production rates reported here at 280–400 °C are comparable, and even faster than those documented for serpentinization of olivine and harzburgite. A major feature of arfvedsonite alteration in peralkaline plutons is the formation of aegirine as a replacing mineral. However, aegirine was never observed in the reacted solids from our experiments, under the condition tested (up to 400 °C and 400 bar). This may be an effect of pressure, oxygen fugacity, or reaction progress, parameters that remain to be investigated to better constrain the reaction mechanism of

arfvedsonite alteration. Agpaitic peralkaline igneous intrusions thus represent a fertile geological setting for deep microbial subsurface ecosystems, abiotic synthesis of organic molecules, and natural H_2 exploration for an alternative source of energy.

1. Introduction

Production of molecular hydrogen (hereafter hydrogen or H_2) is a phenomenon that can occur naturally during water-rock interaction (Klein et al., 2020). Recently, this process has drawn increasing scientific attention owing to the central role that this molecule plays in supporting deep microbial subsurface ecosystems and in promoting abiotic synthesis of organic molecules (Ménez et al., 2020; Sleep et al., 2004; Truche et al., 2020). Furthermore, in the last couple of years, growing pressure on our society to develop carbon-free technology has sparked an unprecedented interest in naturally occurring H_2, as it could represent a potential alternative resource to fossil fuels (Donzé et al., 2020; Gaucher, 2020; Murray et al., 2020; Prinzhofer et al., 2018; Truche and Bazarkina, 2019, Smith et al., 2005). Spontaneous production of H_2 in nature involves nonbiological processes in the Earth's crust, driven by reactions such as (1) reduction of water during the oxidation of iron in minerals (Klein et al., 2013, McCollom et al., 2016; McCollom et al., 2020a; Milesi et al., 2015), (2) radiolysis of water due to radioactive decay of U, Th, and K (Lin et al., 2005; Truche et al., 2018), (3) reaction of water with surface radicals during mechanical fracturing of silicate-bearing rocks (Hirose et al., 2011), and (4) reaction of FeS with water to generate FeS_2 plus H_2 (Drobner et al., 1990). Among these reactions, the most thoroughly investigated has been undoubtedly those taking place during hydrothermal alteration of ultramafic rocks (i.e. serpentinization), where hydration of Fe^{II}-bearing olivine and pyroxene leads to the concomitant reduction of water into H_2 (Cannat et al., 2010; Klein et al., 2020; Worman et al., 2016, 2020). The numerous occurrences of H_2-bearing fluids documented in ultramafic geological environments such as mid-oceanic ridges (Charlou et al., 2002; Seewald et al., 2003), ophiolites (Chavagnac et al., 2013; Coveney et al., 1987; Neal and Stranger, 1983; Vacquand et al.; 2018), Precambrian terrains or greenstone belts (Boreham et al., 2021; Sherwood Lollar et al., 2014) have of course motivated these researches.

Less known than the above-mentioned geological contexts, high H_2 contents are also reported in olivine free, agpaitic peralkaline igneous intrusions among which those of Strange Lake (Canada), Ilímaussaq (Greenland), Lovozero and Khibiny (Kola Peninsula, Russia) are world-class occurrences (Krumrei et al., 2007; Marks and Markl, 2017; Nivin, 2019; Potter et al., 2013; Salvi and Williams-Jones, 1992, 2006). In the latter two cases, H_2, together with CH_4 and higher hydrocarbons, in addition of being observed in fluid inclusions entrapped in minerals (up to 40 mol%), also occurs as a free gas phase in fracture networks in the rocks, as well as in underground mine galleries where it poses serious safety issues (Ikorskiy, 1986; Nivin, 2016, 2019, 2020; Nivin et al., 1995; 2001). Such unique occurrences of H_2 occluded in minerals, diffusely dispersed and freely migrating in rock fractures and soils, raise important questions about the source of this gas. The two main processes that have been proposed to account for H_2 production in these rocks rely either on early magmatic degassing (Beeskow et al., 2006; Konnerup-Madsen, 2001; Vasyukova et al., 2016; Vasyukova and Williams-Jones, 2019) or on late subsolidus hydrothermal alteration of ferrous minerals (Salvi and Williams-Jones, 1992, 1997; Potter and Konnerup-Madsen, 2003; Potter et al., 2013; Vasyukova et al., 2016; Vasyukova and Williams-Jones, 2019). The latter hypothesis is supported by fluid-inclusion evidence and by the petrographic observation of pseudomorphic replacement of the Fe^{II}-bearing amphibole arfvedsonite by aegirine, a Fe^{III}-bearing pyroxene, as shown in **Figure 1**. Such a reaction may lead to H_2 production according to:

$$3Na_3Fe^{II}_4Fe^{III}Si_8O_{22}(OH)_2(\text{arfvedsonite}) + 2H_2O = 9NaFe^{III}Si_2O_6(\text{aegirine}) + 2Fe_3O_4 + 6SiO_2 + 5H_2 \quad (1)$$

At Strange Lake, this reaction is interpreted to have been caused by relatively saline orthomagmatic brines released during crystallization of the transsolvus granite at $T \geq 350$ °C (e.g. Salvi and Williams-Jones, 1992; 1996, 1997).

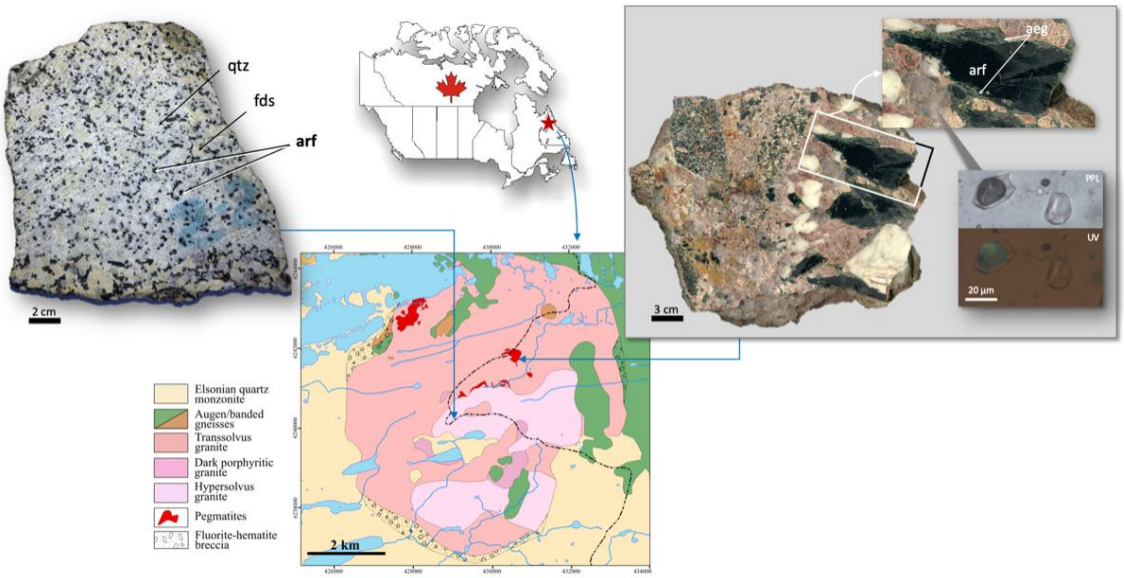

Figure 1. Geological map of the Strange Lake pluton (courtesy of O. Vasyukova) locating the sample of hypersolvus granite used for the experiments (left-hand side). On the right-hand side is shown a sample of altered pegmatite where incipient replacement of arfvedsonite (large dark green crystals) by aegirine (light green) is clearly visible. The fluid inclusions displayed in the inset represent an example of coexisting L- and V-rich individuals, where the latter contain hydrogen as well as higher-order hydrocarbons, showing fluorescence under UV illumination. qtz = quartz, fds = feldspars, arf = arfvedsonite, aeg = aegirine.

Recently, Vasyukova et al. (2016), and Vasyukova and Williams-Jones (2019) documented in more details the fluid evolution of the hydrothermal systems at Strange Lake, on the basis of a meticulous fluid and melt inclusion study. According to these authors, fluid evolution commenced with the exsolution of a brine (~25 wt% NaCl eq.) coexisting with an immiscible CH_4-dominant vapor from a pegmatitic melt, at temperatures of ~450–500 °C and a pressure of ~1100 bar. During isobaric cooling path, the vapor phase gradually evolved from CH_4-dominant to a CH_4-bearing mixture with a significant proportion of H_2 and higher-order hydrocarbons. Formation of C_2 to C_6 hydrocarbons, and at least part of the hydrogen, was synchronous to the alteration of arfvedsonite to aegirine and occurred at ~325–360 °C. The last stage of fluid evolution – after cessation of arfvedsonite alteration – is characterized by a CO_2-dominant fluid at ~300 °C. Along this temperature-pressure paths, the apparent

salinity of the aqueous fluid decreased from ~25 to ~4.5 wt% NaCl eq. due to fluid-rock interaction.

Based on this knowledge, we constructed an experimental study that, for the first time, reproduces the production of H_2 by altering arfvedsonite from peralkaline granite. As starting material, we used separate arfvedsonite grains and whole granite samples from the Strange Lake pluton and, by controlling temperature, pH and salinity of the fluid we obtained the amounts, rate and mechanisms of H_2 generation between 280 and 400 °C at various pressures. These results are compared to available experimental data on H_2 generation during serpentinization of olivine and ultramafic rocks. Our findings provide new, important insights into H_2 generation during the interaction of aqueous fluids with peralkaline rocks.

2. Experimental Methods

2.1. Materials

A sample of unaltered peralkaline granite from Strange Lake (Canada), hereafter noted SL-granite, was used as a starting material for all experiments (**Fig. 1**). This granite, of hypersolvus composition, represents the earliest and least evolved intrusive facies of the pluton (Siegel et al., 2018). The sample was collected from an outcrop in the southern parts of the pluton, a unit known to be unattained by hydrothermal alteration (e.g. Salvi & Williams-Jones 1990; Siegel et al., 2018). Attention was also payed to eliminate all parts that were exposed to weathering. The unaltered nature of the sample was verified by petrographic observations. The modal mineralogical composition of SL-granite, deduced by X-Ray diffraction (XRD) analysis, is as follows: 33 ±2 wt% albite, 28 ±2 wt% microcline, 28 ±2 wt% quartz, 10 ±2 wt% arfvedsonite, 0.6 ±0.2 wt% fluorite, and minor rutile. Aegirine was neither detected by XRD analysis nor by any other technique used in this study.

The SL-granite sample was ground with an agate mortar, sieved (53–212 μm), sonicated in Milli-Q water (resistivity of 18.2 MΩ.cm at 25 °C) to remove adhering fine particles, and dried in a glove box under inert argon atmosphere ($[O_2]$ < 1 ppm) at room temperature. Arfvedsonite and quartz were recovered separately using a hand magnet and hand-picked under a binocular microscope, respectively. Quartz was used in some blank experiments to evaluate possible sources of H_2. Once separated, the solids were washed with 1 M HCl, rinsed several times with Milli-Q water and stored under anoxic conditions (using Ar gas) in a glove box ($[O_2]$ < 1 ppm). The chemical composition of arfvedsonite was obtained by electron microprobe analysis (**Supplementary Table S1**) and its Fe^{3+}/Fe^{2+} ratio was measured by Scanning Transmission X-Ray microscopy (STXM - see analytical methods below). Based on these data and using the methods proposed by Li et al. (2020), we obtained the following arfvedsonite formula:

$$[Na_{2.87}K_{0.51}][Fe^{2+}_{3.0}Mn_{0.07}Ca_{0.02}; Fe^{3+}_{1.45}Al_{0.06}][Si_{7.96}Ti_{0.09}Zr_{0.009}]O_{22}(OH)_{1.87}F_{0.13}$$

The BET surface areas of SL-granite and arfvedsonite measured using Kr as the adsorbate gas are similar: 0.30 ± 0.03 $m^2\ g^{-1}$.

2.2. Experiments

2.2.1. Experimental Strategy

Initially, we performed a number of blank experiments to ensure that all hydrogen measured was produced from the experimental charges, and, conversely, that no hydrogen escaped the experimental systems. More details on blank runs are provided in subsequent sections. To test the potential effect of minerals other than arfvedsonite, in addition of using arfvedsonite-only powders we also ran experiments using whole SL-granite. Experiments were carried out at 280 to 400 °C, in order to cover the expected temperature range at which arfvedsonite is

interpreted to be replaced by aegirine in nature (Salvi and Williams-Jones, 1992; 1996, 1997, 2006; Potter et al. 2013). For similar reasons, the pressure during the experiments ranged from 70 to 500 bar. A parametric investigation of the effect of pH and salinity was performed at 350 °C and 500 bar. A salinity of 3 m NaCl (i.e. 17.4 wt% NaCl) was chosen to reproduce those measured in fluid inclusions (Vasyukova et al., 2016). Finally, as the pH of the fluids responsible for the alteration of the Strange Lake granite was quite variable (i.e., ranged from 3 to 10; Vasyukova and Williams-Jones, 2019), we investigated very contrasted pH conditions using 0.1 m HCl (pH = 1) or 0.1 m NaOH (pH = 13) starting solutions. The pH value was free to evolve over the course of the experiments but, regardless, such acidic or alkaline solutions impose drastically different pH conditions.

Two experiments were designed to measure the rate of H_2 production during SL-granite alteration. One experiment was carried out at 280 °C and 70 bar, in the presence of SL-granite and pure water. Another experiment, performed at 350 to 400 °C, was designed to study the effect of salinity and fluid density on H_2 production rate. This experiment aimed at reproducing the vapor-liquid immiscibility that occurs when adiabatically decompressing a supercritical brine from 400 °C/400 bar to 400 °C/260 bar. The sections below detail the experimental setups and conditions.

2.2.2. Experiments performed at 350°C/500 bar in gold capsules

A set of 17 experiments were carried out in gold capsules loaded in cold-seal pressure vessels and reacted at 350 °C and 500 bar for 15 days (360 hours) (runs #1 to #15 in **Table 1**). The experimental charges consisted of ~50 mg of solids (SL-granite, arfvedsonite, or quartz) and ~50 mg of solution (milli-Q water, or 3 m NaCl brines ± 0.1 m HCl ± 0.1 m NaOH). Blank experiments without solid (fluid only) or without fluid (solid only) were performed to quantify possible background H_2 generation due to Au capsule oxidation, or released from

minerals. The Au capsules (volume of ~0.2 mL) were filled under anoxic condition inside a glove box under Ar atmosphere ($[O_2] < 1$ ppm), and their extremities were pinched shut before extracting them out of the glove box. The capsules were then immediately welded and placed inside an oven at 90 °C overnight to ensure absence of leakage (the mass of the capsules was weighted before and after heating). For the experiment, the capsules were loaded into a cold-seal pressure vessel filled with water as the pressure medium, pressurized at 500 bar and heated to 350 °C for 15 days. After reaction, the autoclaves were quenched with a flux of compressed air for up to 15 minutes and opened. The Au capsules were weighted again to verify leakage had not occurred. A syringe equipped with an indenter and a three-way valve was used to pierce the Au capsules and to release the produced gas. The syringe was previously flushed with Ar to remove air. The gas mixture (Ar + released gases) was sampled through a septum placed on one of the valve's taps and analyzed by gas chromatography for H_2, CO_2 and CH_4. All details of gold capsule piercing, gas recovery and analysis are described by Malvoisin et al. (2013). The pH and chemical composition of the reacted fluids were not measured in these experiments because of the difficulty in retrieving sufficient amount of fluid after capsule piercing and gas analysis. The solids were recovered and immediately transferred into the anoxic glove box where they were rinsed with milli-Q water, dried at ambient temperature under Ar atmosphere and stored until the time of analysis.

Table 1: List of experiments and conditions.

#run	Initial fluid composition	Starting material	Experimental setup	T (°C)	P (bar)	W/R mass ratio
1	- (dry)	SL-granite	gold capsule	350	500	no solution
2	- (dry)	arfvedsonite	gold capsule	350	500	no solution
3 and 3’	H_2O	SL-granite*	gold capsule	350	500	1
4 and 4’	H_2O	arfvedsonite*	gold capsule	350	500	1
5	H_2O	no solid	gold capsule	350	500	no solid
6	3 m NaCl	SL-granite	gold capsule	350	500	1
7	3 m NaCl	arfvedsonite	gold capsule	350	500	1
8	3 m NaCl	quartz	gold capsule	350	500	1
9	3 m NaCl	no solid	gold capsule	350	500	no solid
10	3 m NaCl + 0.1 m HCl	SL-granite	gold capsule	350	500	1
11	3 m NaCl + 0.1 m HCl	arfvedsonite	gold capsule	350	500	1
12	3 m NaCl + 0.1 m HCl	no solid	gold capsule	350	500	no solid
13	3 m NaCl + 0.1 m NaOH	SL-granite	gold capsule	350	500	1
14	3 m NaCl + 0.1 m NaOH	arfvedsonite	gold capsule	350	500	1
15	3 m NaCl + 0.1 m NaOH	no solid	gold capsule	350	500	no solid
QTZ280	H_2O	Quartz	Ti autoclave	280	70	20
SL1	H_2O	SL-granite	Ti autoclave	280	70	20
SL9	H_2O	SL-granite	flexible-cell autoclave	350 → 400	400 → 260	10

“” indicates that the experiment was replicated, “m” stands for molality in mol kg_w^{-1}*

2.2.3. Experiments performed at 280 °C in a batch autoclave

Two experiments were conducted in a 450-mL Parr® stirred batch hydrothermal reactor made of pure titanium (Ti grade 4). The reactor was equipped with several connections that enable periodic on-line sampling of reaction liquid (Ti sampling line fitted with a 1 µm Ti porous filter) and gas, to monitor reaction progress. The autoclave was heated

in air at 400 °C for 48 hours to make sure all surfaces were oxidized prior to the experiment to form a quasi-inert TiO_2 passivated layer. The investigated system was composed of 300 g of Milli-Q water and 15 g of powdered (53–212 μm) SL-granite (#SL1) or pure quartz (#QTZ280), for an initial water-to-rock mass ratio (W/R) of 20 (**Table 1**). The experiment conducted with pure quartz was used as a blank to monitor background H_2 production from eventual autoclave corrosion or fluid inclusion decrepitation. The reaction vessel was bubbled and flushed with Ar to ensure anoxic condition prior to heating. The reactor was then rapidly heated to 280 ±1 °C within 15 min. The experiments were conducted at 70 bar total pressure and 280 °C, during 4 weeks. This pressure resulted from the vapor pressure (64 bar at 280 °C) plus the background Ar pressure that ensured anoxic condition and leakage detection during the run. The calculated partial pressures of H_2, CO_2 and CH_4 produced during the experiment remained < 0.2 bar during the entire run.

Liquid and gas were sampled regularly throughout the experiments. During each sampling, three separate liquid aliquots were collected for a total volume of ~6 mL. The first aliquot allowed purging of the sampling line. The second aliquot was used for pH measurements. Total dissolved cations (Ca, Na, K, Mg, Al, Si, Fe, Mn) were determined from the third aliquot, after filtration at 0.2 μm and HNO_3 dilution. Gas was sampled directly into a gas-tight, Ar-purged glass syringe and analyzed by gas chromatography for the abundance of H_2, CO_2 and CH_4. Each successive sampling induced a slight pressure decrease – from 70 to 66 bar over the entire duration of the experiments. Necessary corrections were made to calculate the total amount of H_2 produced by considering the volume of liquid and gas sampled, the remaining volume of liquid or gas in the reactor at each step, and the pressure change. The amount of H_2 dissolved in the aqueous phase was calculated using the Henry's law constant at water saturation pressure reported by Fernández-Prini et al. (2003): $Log_{10}(k_H/MPa) = 1.88$ at 280 °C and P_{sat}. After reaction, the autoclave was quenched in cold

247 water and opened. Solids were immediately transferred into a glove box, rinsed with Milli-Q
248 water and then dried at room temperature.
249
250 *2.2.4. Experiments performed at temperatures ranging from 350 to 400 °C in a flexible-cell*
251 *hydrothermal autoclave*
252 One experiment (#SL9) was carried out in a flexible-cell hydrothermal apparatus
253 (CoreTest®) using a 155 mL flexible titanium reaction cell fitted with a titanium sampling
254 line (1 µm Ti porous filter, Ti tube and valve). All titanium components were heated in air for
255 at least 48 hours at 400 °C prior to the experiment in order to form a relatively inert TiO_2
256 surface layer. The reaction cell was contained within a stainless-steel pressure housing, with
257 water used as an external pressurizing fluid. The external pressurizing water was spiked with
258 1 mmol L^{-1} $SrCl_2$, and the concentration of Sr inside the flexible Ti cell was monitored over
259 the course of the experiment to test for leakage. The reaction cell was initially loaded with 7.3
260 g of SL-granite of uniform grain size (53–212 µm) and 73 g of Milli-Q water - W/R = 10
261 (**Table 1**). Fluids were sampled during the experiments in order to monitor reaction progress
262 over time. At each instance, two separate aliquots were sampled for a total mass of fluid of 3
263 to 7 g. The first one corresponded to the sampling of the purge line and the second one was
264 used for gas and total dissolved cation analysis. These samples were collected in two separate
265 titanium cells previously evacuated (primary vacuum). The pressure was returned to the
266 targeted value after each sampling point. This experiment consisted of 3 consecutive stages:
267 1) 350 °C and 400 bar, for 336 hours; 2) 400 °C and 400 bar, for 216 hours; and finally 3) 400
268 °C and 260 bar, after NaCl-bearing solution injection, for 210 hours. During the first two
269 stages of the experiment (up to 400 °C and 400 bar), the reaction occurred in a single-phase
270 fluid. The flexibility of the Ti reaction cell allowed fluids to be sampled without loss of
271 pressure and eliminated the presence of a vapor headspace so that reactions remained

confined to the aqueous phase. The density of the fluid decreased slightly, from 0.67 to 0.62 g cm^{-1}, from stage 1 to stage 2 (single-phase fluid). In contrast, the last stage was conducted in the presence of two fluid phases: brine and vapor. Ten milliliters of a 5 molar NaCl brine were injected inside the Ti flexible cell at 400 °C and 400 bar by means of a high-pressure hand (capstan) pump. After brine injection, the pressure decreased to 260 bar, inducing phase separation. The respective density, volume and salinity of the brine and vapor phases were as follow: 0.70 g cm^{-1} / 16 mL / 2.7 m NaCl, and 0.19 g cm^{-1} / 89 mL / 0.028 m NaCl. During this last stage, only the vapor phase was sampled to avoid damaging the flexible cell and strong fluctuations of the W/R ratio. After reaction, the autoclave was quenched with a flux of compressed air for up to 20 minutes and opened. Solids were immediately transferred into the glove box, rinsed with Milli-Q water and then dried at room temperature.

2.3. Analytical techniques

2.3.1 Gas and liquid analysis

The gas samples were analyzed using a Perkin Elmer® CLARUS 500 gas chromatograph (GC) equipped with a thermal conductivity detector (TCD) and a 2-m long column (RESTEK® Shin Carbon ST 80/100) traversed by Ar as carrier gas. The GC was calibrated using several Ar+H_2+CH_4+CO_2+CO gas mixtures of different concentrations injected with a gas syringe of calibrated volume. The estimated analytical error is ± 5 %. In most cases the reported H_2, CO_2 and CH_4 concentration are averages of 3-4 gas injection into the GC. For comparative purposes, the measured H_2 concentrations were normalized to the total number of moles of H_2 generated per gram of SL-granite or arfvedsonite to account for variations in the amount of solid reactants used in different experiments and for the changing mass of fluid present in the reaction vessel as aliquots are removed during sampling.

Liquid aliquots from experiments carried out in Ti autoclaves (both Parr and Coretest) were filtered (0.2 μm), diluted and acidified (2 vol. % HNO_3), and analyzed for major cations with matrix-matched standards using inductively coupled plasma-atomic emission spectroscopy (ICP-AES; Varian® 720ES) with a precision of 3 % at the 95 % confidence level. Fluid chemistries as analyzed and corrected for acid dilution are reported in **Supplementary Tables S2**.

2.3.2. Electron microscopy

Scanning Electron Microscopy (SEM) was used for examination of the morphology and texture and for chemical investigation of the powdered samples before and after reaction. SEM images were obtained using a Tescan® Vega3 electron microscope operating at 15 kV, equipped with an Energy Dispersive X-ray Spectrometer (EDXS). Photomicrographs were recorded both in secondary (SE) and backscattered (BSE) electron modes.

Additional compositional data were obtained by Electron Microprobe Analysis (EMPA) using a JEOL® JXA 8230 electron microprobe equipped with five wavelength-dispersive spectrometers. Arfvedsonite was analyzed with an accelerating voltage of 15 kV, a beam current of 12 nA and a defocused beam diameter of 5 μm. The standardization was made using natural minerals and synthetic oxides standard set (P&H Developments Ltd.). The Smithsonian hornblende USNM143965 (Jarosewich et al., 1980) was measured as an unknown together with our samples to verify analytical accuracy and precision.

Transmission Electron Microscopy (TEM) micrographs and Energy-dispersive X-ray (EDX) analysis were obtained on thin section cut with a Focused Ion Beam (FIB). The areas of interest were milled with a FIB in order to obtain ultrathin samples – with conservation of the texture of the mineral phases – transparent to the TEM electrons. This was done on a cut oriented vertically and perpendicular to the sample surface, using the FEI strata DualBeam

235 of Institut d'Electronique, de Microélectronique et de Nanotechnologie (IEMN, Lille), and cut out to a size of approximately 15 µm by 5 µm and a thickness around 80 nm. Such preparation allows a cross sectional view of the altered material. To check the preservation of the mineral crystalline structure after FIB milling, lattice-fringe imaging was systematically carried out with the TEM, following the protocol of Bourdelle et al. (2012). The FEI Tecnai® G2-20 model TEM used (Plateforme de Microscopie Electronique de Lille (PMEL) – Institut Chevreul of Lille, France) operates at 200 kV, and is equipped with a Charged-Coupled Device (CCD) camera and an EDX spectrometer allowing to acquire chemical analysis (on 50 nm diameter surface area) with a counting time of 30 s for a dead time of less than 10 %.

2.3.3. X-ray diffraction

Powder X-ray diffraction (XRD) patterns were acquired from both random and oriented mounting of the samples. The diffractometer was a Bruker® D8 equipped with a SolX Si(Li) solid state detector from Baltic Scientific Instruments using CuKα radiation (λ = 1.5406 Å) generated at 40 kV and 40 mA. On the primary side, a divergence slit (0.298°) and a soller slit (2.5°) were used, while on the secondary side an antiscattering slit (0.298°), a soller slit (2.5°) and a receive slit (0.06°) were used. Intensities were recorded at 0.026°2θ step intervals from 5 to 90° (5 s counting time per step) and from 2 to 50° (4 s counting time per step) for bulk and clay mineralogy determination, respectively. The bulk mineralogy was determined on the <2 mm fraction (obtained after grinding the samples using a McCrone® micronizing mill). The clay mineralogy was determined on the <2 µm fraction. Following sonication of the samples, this fraction was extracted by centrifugation. Oriented mounts were prepared by drying the resulting suspension onto glass slides. Ethylene-glycol (EG) solvation of the slides was achieved by exposing them to EG vapor at 50 °C for a minimum of 12 h. Estimates of modal abundance of minerals were performed using the Rietveld refinement

346 method using the BGMN computer program (www.bgmn.de), based on the XRD patterns
347 collected on randomly oriented samples.

348

349 *2.3.4. STXM-XANES*

350 X-ray adsorption near-edge structure spectroscopy (XANES) data were acquired using
351 the Scanning Transmission X-ray microscope (STXM) of the PolLux beamline (for details
352 about the beamline, see Raabe et al., 2008) at the Swiss Light Source (Paul Scherrer Institute
353 – SLS, Switzerland) and the HERMES beamline (Belkhou et al., 2013) at the SOLEIL
354 synchrotron (France). During data collection, the SLS and SOLEIL synchrotron storage rings
355 operated at 2.4 GeV / 400 mA current and 2.75 GeV / 450 mA current, respectively. STXM
356 allows to collect XANES data on crystallites with a thickness < 100 nm to allow X-ray
357 transmission. The thin crystallites of arfvedsonite were recovered in each reaction product,
358 and dispersed in ethanol; a drop of which is placed (then evaporated) on a carbon holey
359 support film placed on a TEM 200 mesh copper grid. Stacks of images were obtained by
360 scanning – with a spatial resolution of 30 nm – the area of interest in the x–y direction over
361 the 700–730 eV energy range (Fe $L_{2,3}$-edge). Each image of a stack was recorded at one
362 energy, so that the compilation of the same pixel on each image gives one spectrum. Spectra
363 were extracted from stacks using the aXis2000 software (Hitchcock, 2012) and processed
364 following the protocol of Bourdelle et al. (2013). Data were recorded using a circularly
365 polarized light and a dwell time per pixel and energy point of 10 ms.

366 Spectra acquired through the Fe $L_{2,3}$-edge energy range were used to estimate the
367 $Fe^{3+}/\Sigma Fe$ ratio with an uncertainty around 5 %. This estimate of $Fe^{3+}/\Sigma Fe$ ratio is extracted
368 from the ratio of the two (L_3-b and L_3-a) major peak intensities, following the calibration of
369 Bourdelle et al. (2013). This calibration was established on standard samples, all silicates: five
370 iron-silicate glasses (containing various Fe^{3+} contents), eight phyllosilicates (several chlorites,

micas and smectite with various Fe^{3+} contents) and a fayalite. This calibration is not dependent on the silicate structure. To evaluate the result reproducibility, 2 or 3 crystallites of each sample were analyzed, and for each of them 2 to 3 spectra were extracted (i.e. 4 to 6 spectra per sample).

3. Results

3.1 H_2 generation from alteration of peralkaline granite and of pure arfvedsonite at 350 °C, 500 bar

A total of 15 experiments were carried out in gold capsules at 350 °C and 500 bar during 15 days (360 hours) in order to evaluate the effect of both pH and salinity on H_2 generation from peralkaline granite and pure arfvedsonite hydrothermal alteration. Some of these experiments were replicated twice to ensure good reproducibility of the measurements (**Table 1**, **Fig. 2**). As for potential H_2 loss, the very low H_2 permeability of gold below 350 °C has been previously demonstrated (Chou, 1986; Malvoisin et al., 2013). Particular attention was paid at evaluating blank conditions of our experiments, *i.e.*, test whether H_2 could be produced from oxidative dissolution of the gold capsules, fluid inclusion decrepitation, or by releasing of gases occluded in the minerals. We therefore designed a series of runs to determine possible background blank values. The total amounts of H_2 produced during blank experiments are shown in **Figure 2a**.

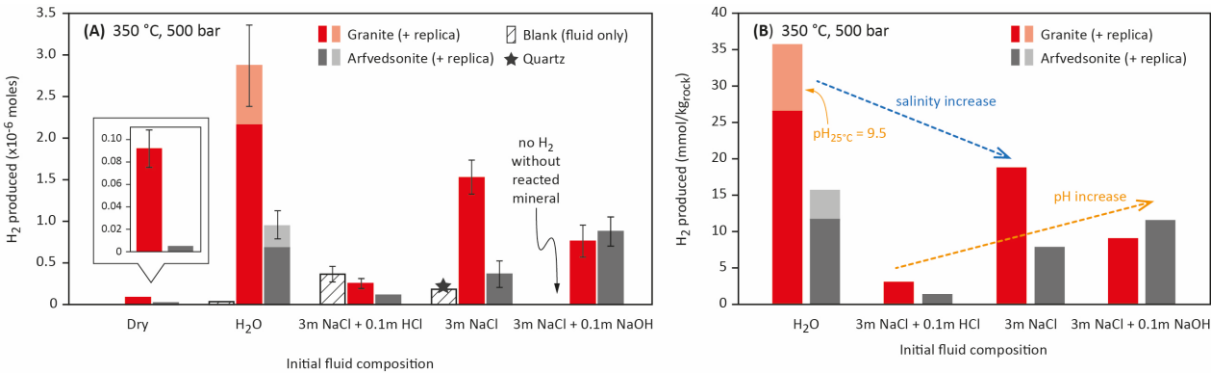

Figure 2. Production of H_2 after 360 hours elapsed time in the gold capsule experiments carried out at 350 °C and 500 bar. Different initial fluid compositions were tested to evaluate the effect of pH and salinity. (a) Experiments carried out in the presence of SL-granite (red) or arfvedsonite (black) are compared to the blanks: fluid only (dashed lines) or quartz + 3 m NaCl (grey star). The notation "dry" indicates that the gold capsule was loaded with solid material only (no fluid). The 2 replicates performed in the presence of water + SL-granite or arfvedsonite are shown in light red and light grey, respectively. (b) Production of H_2 normalized to the mass of solids (SL-granite or arfvedsonite) as a function of fluid composition. Error bars reflect the cumulative uncertainty associated with measuring the volume of gas released after piercing the gold capsules and with the analytical uncertainty.

Hydrogen production from gold capsule oxidative dissolution (Equation 2) was measured as a function of pH in a 3 m NaCl brine (no solid loaded in the capsule).

$$Au(s) + 2Cl^- + H^+ = AuCl_2^- + 0.5H_2(g)$$

The amount of H_2 produced by gold dissolution increased when pH decreased. The concentration of dissolved hydrogen was below the detection limit under alkaline condition (0.1 m NaOH + 3 m NaCl), but reached 8.6 ±0.2 × 10^{-4} m at 350 °C and 500 bar in 0.1 m HCl + 3 m NaCl solution. Such a concentration is in very good agreement with thermodynamic predictions using the HCh software (Shvarov, 2008), based on the stability constant reported by Stefansson and Seward (2003) for the chloridogold(I) complex ($m_{H2(aq)}$ = 6.3 × 10^{-4} m at 350 °C and 500 bar in equilibrium with native Au in a 0.1 m HCl + 3 m NaCl solution).

Under acidic condition, H_2 production recorded during SL-granite and pure arfvedsonite hydrothermal alteration experiments was so low that it can be simply explained by the oxidative dissolution of the gold capsule alone (**Fig. 2a**). However, under

416 circumneutral to alkaline conditions, H_2 produced by gold dissolution represents only a
417 negligible fraction of the total amount of H_2 generated during hydrothermal alteration of SL-
418 granite and pure arfvedsonite (**Fig. 2a**).

419 Blank experiments performed under dry condition (powdered SL-granite or
420 arfvedsonite loaded without water in the gold capsules), or only with quartz from SL-granite
421 reacted with 3 m NaCl brine, revealed that the release of pre-existing H_2 from gases occluded
422 in the minerals or entrapped in fluid inclusions is also negligible. Indeed, less than 5 % of the
423 total amount of H_2 produced in the experiments where SL-granite or pure arfvedsonite were
424 hydrothermally reacted can be attributed to pre-existing H_2.

425 To better compare the effect of pH, salinity and mineralogical assemblage, the total
426 amounts of H_2 produced during both SL-granite and arfvedsonite-bearing experiments were
427 normalized to the mass of solid initially introduced inside the gold capsules (**Fig. 2b**). Clearly,
428 H_2 production was promoted by circumneutral to alkaline conditions. The maximum amount
429 of H_2 produced was recorded after reaction of SL-granite with water: from 27 to 36 mmol
430 kg_{rock}^{-1} of H_2 were produced within 15 days (**Fig. 2b**). Note that hydrothermal alteration of
431 SL-granite naturally imposes alkaline conditions ($pH_{25°C}$ = 9.5 and 8.2 were measured after
432 runs #SL1 and #SL9 carried out at 280 °C and 400 °C, respectively - see below). Altogether,
433 these experiments demonstrated that H_2 production from the hydrothermal alteration of SL-
434 granite and of pure arfvedsonite strongly depends on pH. The comparison of experiments
435 conducted with and without dissolved NaCl reveals that salinity decreases the production of
436 H_2, by 10 to 40 %. Comparatively, SL-granite alteration produced more H_2 than arfvedsonite
437 alone.

438 Carbon dioxide and CH_4 were also quantified in the gold capsules after 15 days of
439 reaction (**Fig. 3**). As expected, neither of these species were detected in the experiments
440 conducted with fluid only (no solid charge). Remarkably, in runs where SL-granite or

arfvedsonite were reacted, the presence of fluid did not seem to have an impact on CO_2 and CH_4 production, as both molecules were detected in similar amounts under dry condition (**Fig. 3a, b**). This observation contrasts with the near absence of H_2 released under dry condition (**Fig. 2**). The mineralogical assemblage, i.e., SL-granite or arfvedsonite, also has only a weak impact on CO_2 and CH_4 production (**Fig. 3c, d**). Also expected, a clear effect of pH was observed on gaseous CO_2 production under hydrothermal conditions – from 25 to 35 mmol kg_{rock}^{-1} under acidic condition (0.1 m HCl + 3 m NaCl) to less than 6 mmol kg_{rock}^{-1} under alkaline condition (0.1 m NaOH + 3 m NaCl) – but this result can be easily explained by carbonate speciation and CO_2 solubility as a function of pH. Methane on the other hand, was released in a much lower amount: from 2 to 5 mmol kg_{rock}^{-1}, with no clear fluid, mineralogical or pH effect. This notwithstanding, a discussion on the sources of CO_2 and CH_4 is beyond the scope of this study, and these results are provided for information purposes only. We do point out, however, that minerals such as nahcolite and REE (Rare-Earth Elements)-Sr-carbonates have been reported in the hypersolvus granite at Strange Lake and that both CH_4 and CO_2 may be occluded or trapped in melt/fluid inclusions in these minerals (Vasyukova et al., 2016; Vasyukova and Williams-Jones, 2019; Gysi et al., 2013, 2016).

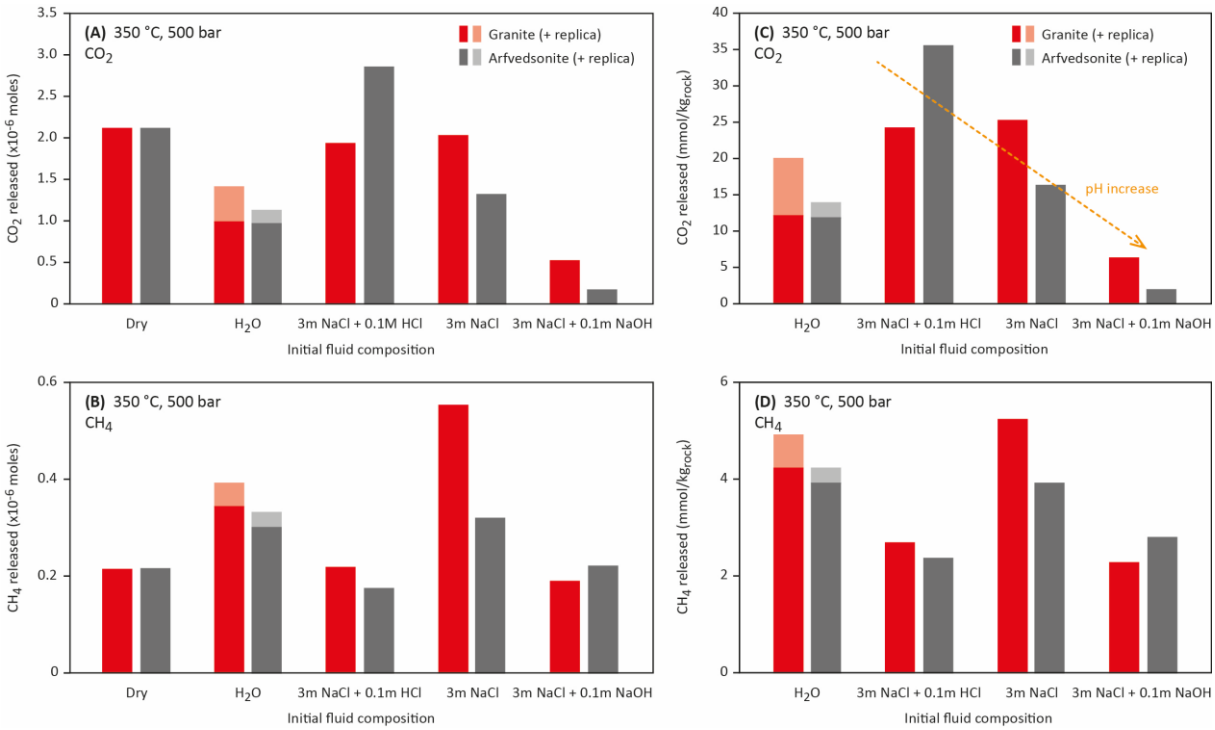

Figure 3. Production of CH_4 and CO_2 after 360 hours elapsed time in gold capsule experiments carried out at 350 °C and 500 bar. (a) and (b) moles of CO_2 and CH_4 produced in the gold capsules as a function of fluid composition, respectively. The annotation "dry" indicates that the gold capsule was loaded with solid material only (no fluid). (c) and (d) show production of CO_2 and CH_4 normalized to the mass of solids (SL-granite or arfvedsonite) as a function of fluid composition, respectively. The orange dashed line depicts a trend of decreasing CO_2 concomitant with increasing pH of the fluid.

3.2 H_2 generation from peralkaline granite alteration at 280 °C and vapor saturation pressure

At 280 °C and vapor saturation pressure, H_2 was produced continually over 650 hours when reacting SL-granite with pure water (**Fig. 4**). After 650 hours had elapsed, H_2 concentration reached 13 mmol kg_{rock}^{-1}. The concentration of CO_2 remained nearly constant at 2 mmol kg_{rock}^{-1} throughout the run, and traces of CH_4 were detected (below the quantification limit of 10 ppm) at the end of the experiment. Note that the total carbonate concentration is unknown as most of the CO_2 is dissolved in the aqueous phase, given the alkaline pH value recorded on the liquid samples throughout the experiment. The concentrations of major dissolved elements (Si, Al, Na, K, Ca, Mg, Mn, Fe) measured throughout the experiment are provided in the **Supplementary Table S2** and the **Figure S1**. No H_2, CH_4 or CO_2 were

detected when reacting the purified quartz fraction from SL-granite under the same condition (#QTZ280, **Supplementary Table S2**).

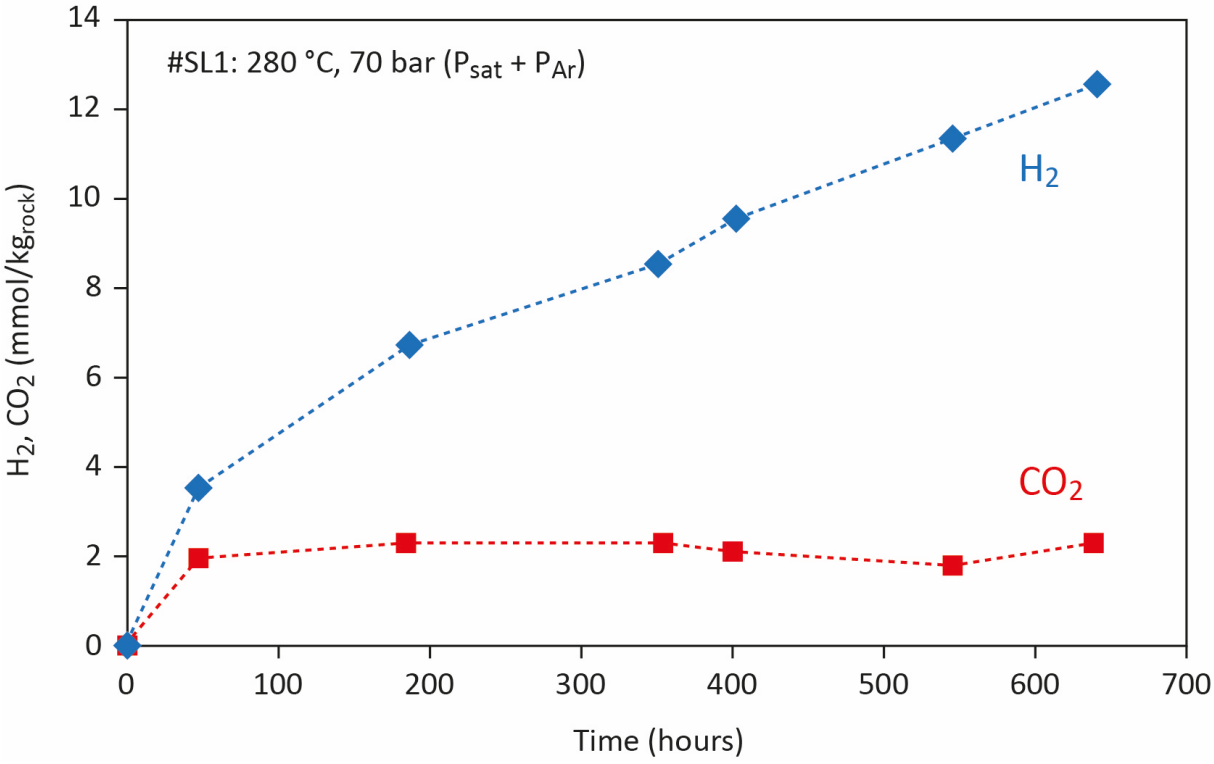

Figure 4. Production of H_2 (blue diamonds) and CO_2 (red squares) as a function of time during experiment #SL1 carried out at 280 °C, 70 bar (Psat + Ar) in the presence of water and SL-granite. Error bars are smaller than the size of the symbols.

3.3 H_2 generation from peralkaline granite alteration up to 400 °C: effect of vapor-brine immiscibility

At 350 °C and 400 bar in a single-phase fluid, H_2 concentration increased rapidly within the first 72 hours of reaction and then followed a relatively constant increase at a slower rate (**Fig. 5**). No significant change in the production rate was observed when temperature was increased from 350 to 400 °C at constant pressure (400 bar). After 552 hours of reaction, NaCl was injected and pressure dropped to 260 bar. Either of these actions alone would have induced phase separation, however, the hydrogen production rate was only

slightly impacted, for a few hours following state change. Despite the fact that a substantial amount of H_2 was generated during the first stage of the experiment, at 350°C and 400 bar, its concentration in the aqueous phase remained well below its solubility threshold, which is ~1.7 m in pure water (Seward and Franck, 1981). Conversely, after phase separation induced by NaCl injection and pressure decrease most of the H_2 was certainly in the vapor phase. Although to this day there is no thermodynamic data to predict the solubility of H_2 in brine nor the vapor/liquid partitioning of H_2 under such condition, it is reasonable to expect the vapor phase to be enriched in H_2 with respect to the liquid phase, due to salting out effect (Bazarkina et al., 2020).

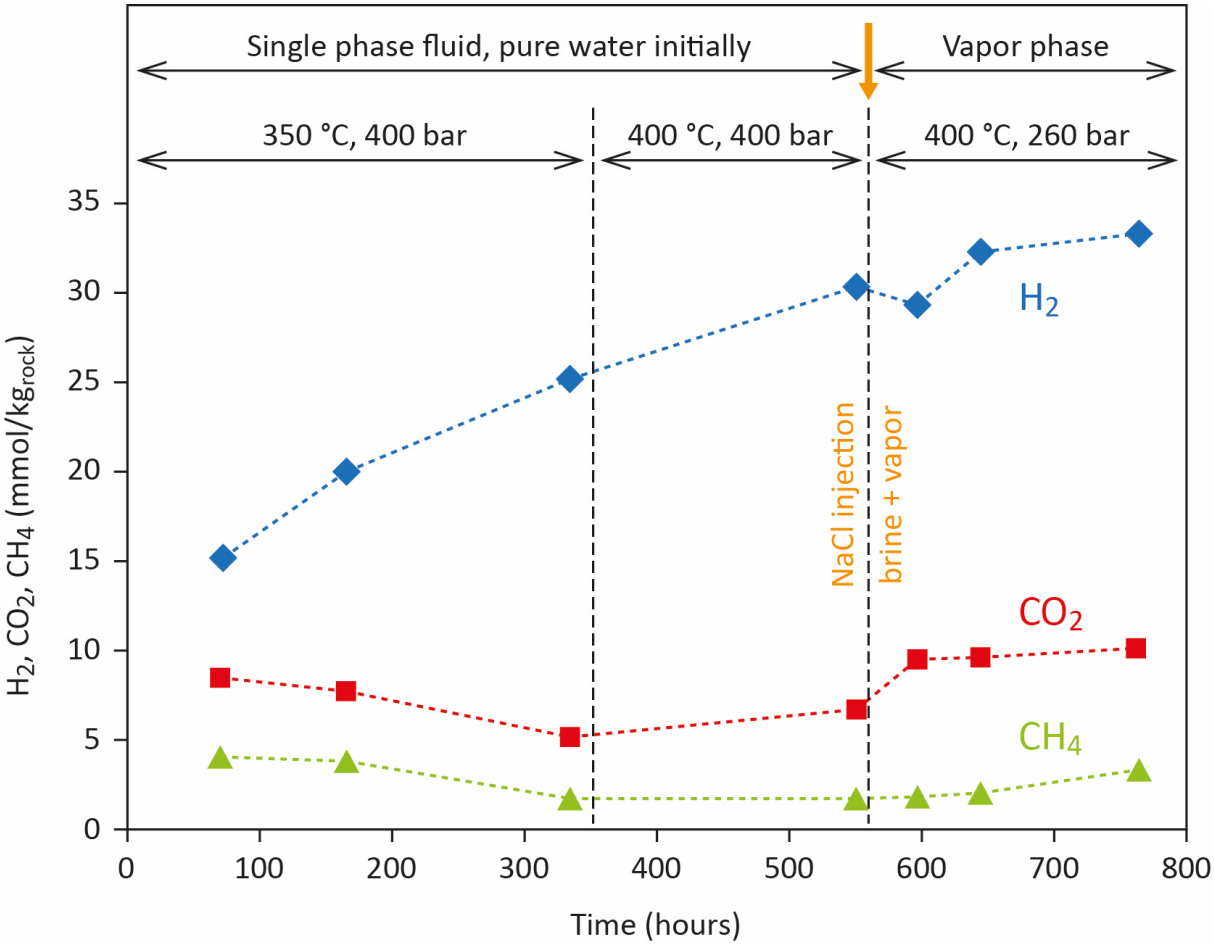

Figure 5. Production of H_2 (blue diamonds), CO_2 (red squares) and CH_4 (green triangles) as a function of time during experiment #SL9 carried out in the presence of water and SL-granite. Temperature, pressure and fluid composition evolve according to 3 consecutive steps as indicated on the figure: 1) 350 °C, 400 bar, pure water initially, then 2) a temperature increase to 400 °C at constant pressure 400 bar, and finally 3) NaCl injection and

pressure decrease to 260 bar at 400 °C. This last step induced phase separation to produce coexisting brine (density = 0.70 g cm^{-1}, 2.7 m NaCl) and vapor (density = 0.19 g cm^{-1}, 0.028 m NaCl). During this stage, sampling was performed from the vapor phase. Error bars are smaller than the size of the symbols.

The concentrations of CO_2 and CH_4 remained relatively constant throughout the experiments, at ~7 and 3 mmol kg_{rock}^{-1}, respectively. Sodium concentrations measured in the vapor phase (~27 mmol kg^{-1}) are in agreement with our thermodynamic predictions (28 mmol kg^{-1}) using the HCh software (Shvarov, 2008). Concentrations of major dissolved elements (Si, Al, Na, K, Ca, Mg, Mn, Fe) measured during the experimental runs are provided in the **Supplementary Table S2** and the **Figure S2**.

3.4 Investigation of solid reaction products

X-Ray diffraction patterns performed on the bulk SL-granite powders, before and after reaction at 280 °C (#SL1) and 400 °C (#SL9) do not provide any clear evidence for the precipitation of secondary minerals (**Supplementary Figure S3a**). After reaction at 280 °C in #SL1 experiment, the most striking feature we observed is extensive dissolution of quartz (**Supplementary Figure S3a**). This observation is consistent with the fact that the reacted solid were cemented in the vessel after this experiment by amorphous silica precipitation. Traces of chlorite (1.8 %), magnetite (0.9 %) and zircon (0.8 %) improved the quantitative analysis (Rietveld refinement) of the XRD pattern collected on solids reacted at 280 °C (#SL1). At 400 °C, magnetite was the only secondary mineral that could be detected by XRD quantitative analysis (0.6 %). However, at such low volumes, identification and quantification of secondary minerals by XRD analysis is challenging. Similarly, no significant mineral neoformation was detected by XRD analysis after reaction of pure arfvedsonite at 350°C, 500 bar in the presence of 3 m NaCl + 0.1 m NaOH (**Supplementary Figure S3b**). However, the X-Ray diffraction patterns collected on the <2 μm fraction recovered after #SL1 and #SL9

experiments confirm the formation of minor chlorite and reveal the presence of other minerals displaying peaks at 11.87, 10.55 and 9.43 ˚2θ (**Supplementary Figure S3c**), which could be assigned to palygorskite and sepiolite. The presence of a hydrous zirconosilicate tentatively identified as catapleiite was also noticed. Experiments carried out at 350 °C in the presence of SL-granite and 0.1 m NaOH (run #13, Table 1), led to the formation of montmorillonite (**Supplementary Figure S3d**). Aegirine was not detected in the reacted SL-granite samples (bulk and clay fraction).

Regardless, extensive SEM analysis performed on all reacted SL granite powders reveals the presence of clear dissolution features at the surface of arfvedsonite at all temperatures investigated (280, 350, 400 °C) under circumneutral to hyperalkaline condition (**Fig. 6**). The dissolution textures are clearly visible along the edges, corners and cleavages of arfvedsonite crystallites. For runs at 280 °C and 350 °C, the surface of recovered arfvedsonite is partially covered by sub-micrometric (< 200 nm) isolated mounds or lumps of a high-density mineral (bright color under BSE mode). Magnetite, another high-density secondary mineral, was also present in the reaction products from all experiments carried out in the presence of SL-granite + H_2O ± NaOH. Magnetite primarily occurs as small (<1 to ~5 μm) euhedral crystals dispersed throughout the reacted solids or coating on the arfvedsonite surface, in particular after reaction at 400 °C (run #SL9). In addition, tiny precipitates of a fibrous mineral are commonly observed on the edge and cleavages of arfvedsonite, for all temperatures investigated. Phyllosilicates displaying two different textures, fibrous and flaky, are observed either at the surface of arfvedsonite or as isolated aggregates, respectively. Most secondary minerals precipitated at the surface of arfvedsonite during the runs are too small for representative EDX analysis, however, in the case of the platy phyllosilicates aggregates, Fe, Mg, K, Na and Al were clearly detected. The presence of chlorite would reconcile this texture with the chemical analyses and the interpretation of the XRD patterns.

When arfvedsonite was reacted alone (350 °C and 500 bar) in pure water or under hyperalkaline conditions, the dissolution features were far less pronounced and no secondary phases were detected at its surface, by SEM observation. Also, no signs of alteration were observed on arfvedsonite in runs done under acidic condition, independently of whether it was alone or embedded within SL-granite.

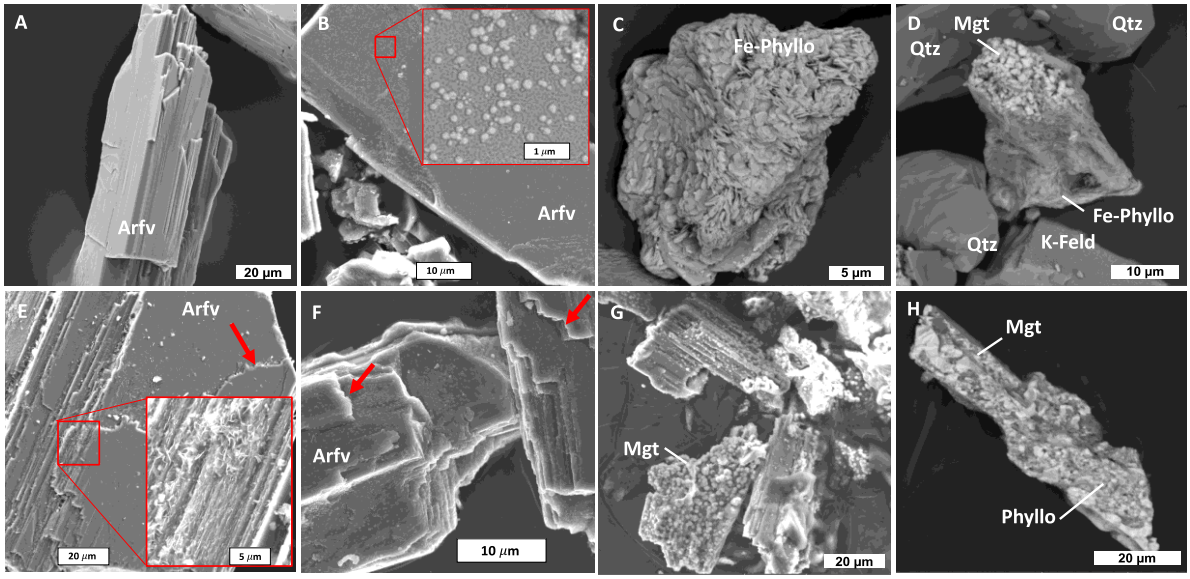

Figure 6. Backscattered electron (BSE) and secondary electron (SE) images of unreacted arfvedsonite and representative reaction products after hydrothermal alteration of SL-granite at 280, 350 and 400 °C. (a) BSE image of unreacted arfvedsonite (Arfv). (b) BSE image of arfvedsonite after reaction at 280 °C (run #SL1) with tiny isolated zircon lumps (<200 nm) on its surface (inset). (c) BSE image of Fe-rich phyllosilicate (Fe-Phyllo) observed in the bulk solids after hydrothermal alteration of SL-granite at 280 °C (run #SL1). (d) BSE images of magnetite (Mgt) crystals imbedded in mats of platy Fe-phyllosilicate after reaction at 280 °C (run #SL1). Quartz (Qtz) and K-feldspar (K-Feld) crystals from SL-granite are also visible. (e) and (f) SE images of arfvedsonite after hydrothermal alteration of SL-granite at 350 °C in the presence of water. The surface of arfvedsonite displays clear dissolution features on the edges, corners and cleavage surfaces (red arrows). The inset in (e) shows the presence of tiny fibrous precipitates along the arfvedsonite cleavages. The surface of arfvedsonite in (f) is also covered with tiny zircon lumps. (g) BSE image of arfvedsonite crystals nearly fully coated by interbedded octahedral magnetite (Mgt) crystals after reaction at 400 °C (run #SL9). (h) BSE image of arfvedsonite crystals fully coated by magnetite and phyllosilicates after reaction at 400 °C (run #SL9).

TEM-EDX observations and analysis performed on FIB ultrathin sections milled perpendicularly to the arfvedsonite surface reacted at 280 °C (#SL1) and 350 °C, ~~initially~~ in the presence of granite and pure water, reveal without any ambiguity that the sub-micrometric

isolated lumps detected by SEM imaging are $ZrSiO_4$ nodules precipitated at its surface (**Fig. 7**). These nodules consist of polycrystalline zircons, with radial growth, constituting half-spheres whose radius does not exceed 200 nm (**Fig. 7d**). They sit on the surface of the arfvedsonite crystallites without crystal connection to them, indicated by the extremely clean and sharp interface between zircon and arfvedsonite (**Fig. 7e, f**). In the same way, zircon nodules seem to precipitate preferentially on large flat and clean arfvedsonite surfaces, rather than in dissolution pits. TEM observations on FIB sections also reveal that monocrystalline arfvedsonite, apart from dissolution areas (edges, corners and cleavages), is not altered, even at the nanoscale, where zircon precipitated (**Fig. 7f**).

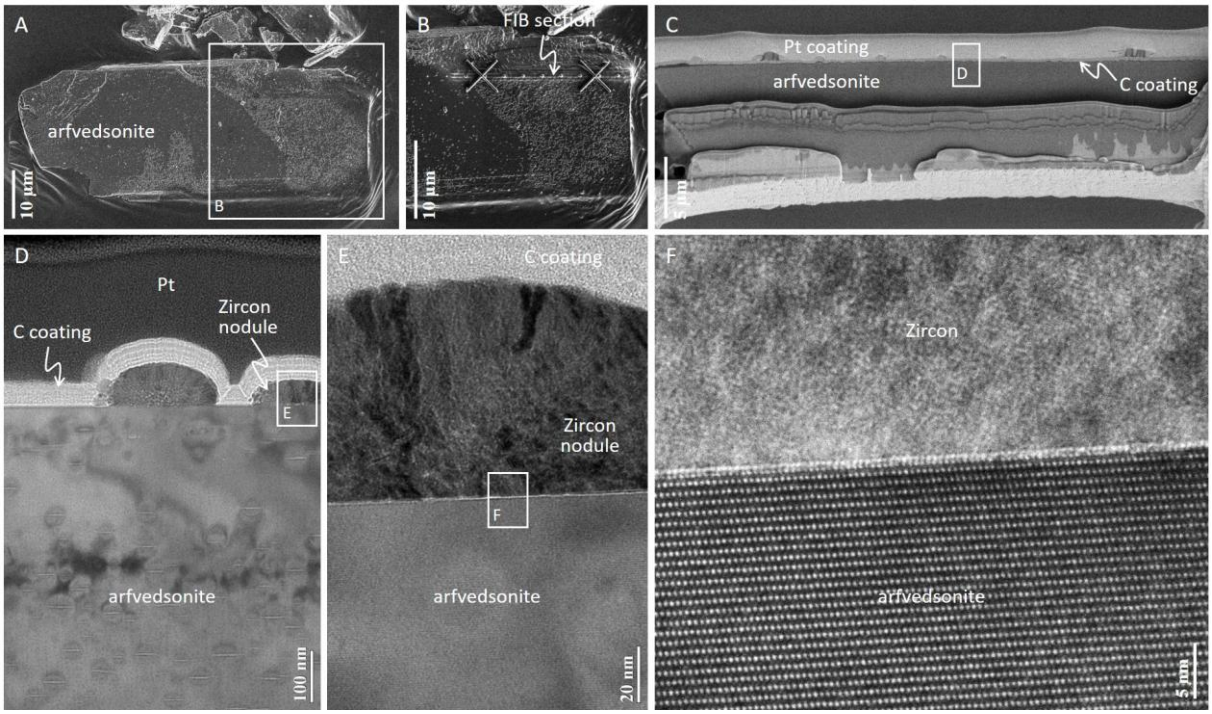

Figure 7. SEM and TEM images of arfvedsonite-zircon nodule interface. (a) SEM image of carbon-coated arfvedsonite crystal covered with nanometric nodules. (b) SEM image of the crystal area targeted for FIB foil cutting. The emplacement of the FIB foil is identified by a platinum deposit (in the shape of a cross and dots). (c) FIB foil extracted from the section defined in (b), with a continuous platinum strap on top of it. The FIB foil presents different cutting thicknesses, the arfvedsonite-zircon nodule interface being the thinnest area. Carbon coating is also visible. (d) Bright-field TEM image of the FIB foil from (c) showing radial-growth of zircon nodules placed on the clean surface of the arfvedsonite crystal. Platinum strap (Pt) and carbon coating are indicated. (e) Expanded view from image (d) presenting a polycrystalline zircon nodule in contact with arfvedsonite. (f) High-resolution TEM image of the interface, showing the crystalline structure of the two phases, with no inter-crystalline connection.

The iron redox state of three arfvedsonite samples – unreacted arfvedsonite and reacted arfvedsonite at 280 °C and at 400 °C (respectively runs #SL1 and #SL9) – was studied by STXM-XANES. The **Figure 8** compares rescaled representative spectra from each sample, corrected for background. Fe $L_{2,3}$-edge spectra display four major peaks, two for the L_3-edge are noted L_3-a (~708.7 eV) and L_3-b (~710.2 eV), two for the L_2-edge are noted L_2-a (~720 eV) and L_2-b (~723.5 eV). L_3-a and L_2-a peaks are mainly affected by the Fe^{2+} content, while the L_3-b and L_2-b peaks are affected by the Fe^{3+} content. Here, unreacted arfvedsonite and #SL1 spectra have a similar shape, i.e. a high L_3-a peak and a small L_3-b peak indicating ferrous phases, while #SL9 spectrum shows an inverted intensity ratio, typical of ferric phases (**Fig. 8**). The estimation of Fe^{3+}/Fe_{total} ratio is based on the L_3-b/L_3-a peak intensity ratio as proposed by Bourdelle et al. (2013), and indicates 33 %, 38 % and 79 % of ferric iron in unreacted, reacted #SL1 and reacted #SL9 arfvedsonite, respectively. These estimates are based on 4 to 6 spectra per samples, showing intrasample homogeneity.

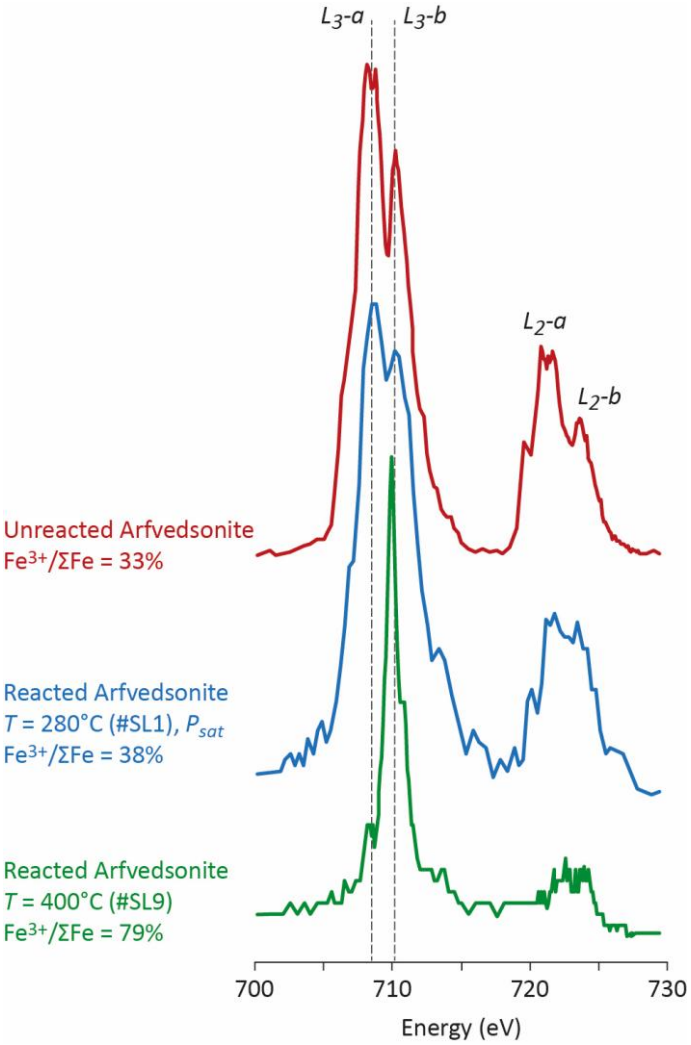

Figure 8. Representative XANES spectra at the Fe $L_{2,3}$-edges for unreacted (in red) and reacted (#SL1 in blue, #SL9 in green) arfvedsonites. Spectra have been normalized to the integral Fe L_3-edge intensity, and shifted vertically for clarity (normalised intensity with arbitrary unit). The vertical dashed lines represent the energies fixed to determine the Fe^{3+}/Fe_{total} ratio from the intensities of L_3-peaks, according to the procedure of Bourdelle et al. (2013).

4. Discussion

4.1 Source of H_2

From the experimental results detailed in the preceding sections, we learned that hydrogen generation in the presence of SL-granite or arfvedsonite occurs under near-neutral to alkaline hydrothermal condition, at $T \geq 280$ °C. A range of blank experiments assessed that no H_2 was produced from the experimental apparatus and that the release of the H_2 occluded

636 in minerals or entrapped in quartz-hosted fluid inclusions from SL-granite was negligible (< 5
637 %). Thus, we can be confident that H_2 in our experiments was indeed produced during water-
638 rock interaction.

639 Production of H_2 occurred when arfvedsonite was the only mineral introduced in the
640 hydrothermal system. Even higher amounts of H_2 were generation when SL-granite
641 (containing 10 wt% arfv) was reacted (**Fig. 2**). The role of granite could either imply that H_2
642 is supplied by more than one source, or that arfvedsonite alteration is enhanced in the
643 presence of other minerals. The presence of Fe is reported in alkali feldspar from the
644 hypersolvus granite, however, it consists of small amounts of ferric iron (0.23 wt% Fe_2O_3, or
645 about 0.01 apfu Fe^{3+} - Siegel et al., 2018), which cannot oxidize to produce H_2. On the other
646 hand, the second hypothesis is more plausible, given that hydrothermal alteration of granite
647 naturally leads to alkaline conditions that, as seen above, favor the H_2-producing reaction. In
648 addition, altering a rock instead of only a mineral will release a range of elements into
649 solution that are likely to enhance precipitation of additional secondary minerals, in particular
650 phyllosilicates. This is consistent with the presence of higher amounts of secondary minerals
651 such as magnetite and phyllosilicates when the granite, instead of arfvedsonite alone, was
652 included in the experimental runs.

653 Experimental replicates performed at 350 °C in gold capsules, using pure water as
654 starting solution, showed a 10 to 30 % difference in the amount of H_2 produced, when
655 comparing two runs carried out under the same conditions. Nevertheless, despite these
656 significant uncertainties on the amount of H_2 produced, a constant result was that alkaline
657 conditions promoted H_2 generation and that salinity of the reacting fluid had a slightly
658 negative impact on H_2 production (**Fig. 2b**). Similar conclusions were drawn recently from
659 laboratory experiments of olivine serpentinization at 200–280 °C (Lamadrid et al., 2017;
660 McCollom et al., 2020b).

4.2. Reaction mechanism

Another question that needs addressing concerns the reaction mechanism of H_2 production. On the basis of petrographic observations, it has been proposed that arfvedsonite is replaced by aegirine under hydrothermal condition at T ≥ 350 °C, and that this replacement releases H_2, according to the **Equation 1** (Salvi and Williams-Jones, 1997; Potter et al., 2013). Replacement of arfvedsonite by aegirine is a common feature of peralkaline rocks (e.g., Marks and Markl, 2017; Bernard et al., 2020), and a beautiful example of arfvedsonite alteration into aegirine is shown in **Figure 1**. In the laboratory, aegirine has been synthesized at temperatures as low as 200 °C in aqueous solutions; below this temperature Na– Fe-phyllosilicates form instead (Decarreau et al., 2004). In our study, however, aegirine formation was not detected, at any of the conditions tested. Possible reasons may include the relatively low pressure (≤ 400 bar) and short duration (< 30 days) of our experiments. Nonetheless, two important lines of evidence demonstrate the occurrence of arfvedsonite oxidative dissolution. Firstly, when observed under an electron microscope, the arfvedsonite surface clearly displays typical features of dissolution, such as dissolved edges and corners as shown in **Figure 6f**. In addition, reacted arfvedsonite is covered by an unexpected multitude of tiny distinct zircon lumps, particularly visible in the experiment carried out at 280 °C and 350 °C in the presence of SL-granite + H_2O (**Fig. 6b, e and f**). In SL-granite, zirconium is present in the form of zircon crystals, but also occurs in the structure of arfvedsonite (EMPA analysis indicate ~1200 ppm). Contrarily to arfvedsonite, primary zircon grains do not show any sign of dissolution. This, together with the fact that the secondary zircon lumps occur only at the surface of arfvedsonite, suggests that Zr was supplied by dissolution of the latter. Because of its extremely low solubility, zircon precipitated at the surface of its source, rather rapidly as suggested by the apparent botryoidal habit of these lumps (**Fig. 7**). A second line of

686 evidence for oxidative dissolution of arfvedsonite is the presence of several Fe^{III}-bearing
687 alteration minerals in the reacted experimental powders. Magnetite was identified on the
688 surface of arfvedsonite and disseminated in the bulk powder, at all investigated temperatures
689 and in the presence of SL-granite + H_2O ± NaOH (**Fig. 6d, g and h**). Phyllosilicates were also
690 detected, their presence confirmed by XRD and SEM analysis (**Fig. 6c, d, e and h**), and
691 display either fibrous or flaky textures (**Fig. 6c and e**). Possibly, chlorite and Na-
692 montmorillonite may also be present, according to some features of the XRD and EDX
693 patterns recorded from SL-Granite reacted at 280 °C. Finally, STXM-XANES analysis
694 revealed a clear increase of the Fe^{3+}/Fe_{total} ratio of the arfvedsonite after reaction at 280 °C
695 and 400 °C (**Fig. 8**). Because the STXM-XANES probes particles trough their thickness, only
696 very thin fragments of arfvedsonite – transparent to X-ray (thickness < 100 nm) – were
697 targeted, i.e. probably the most altered crystallites. Therefore, Fe^{3+}/Fe_{total} values (**Fig. 8**) could
698 be considered either as resulting from structural oxidation of Fe^{II} into Fe^{III}, more detectable in
699 very thin particles, or as an average between a preserved crystal core and an altered ultrathin
700 external layer at the grain surface. The relationship between iron redox estimates and
701 experiment conditions (increasing Fe^{3+} proportions with increasing run temperature) can
702 therefore testify of an ongoing process of arfvedsonite oxidation. This observation may also
703 provide a hint for the absence of aegirine, whose precipitation would supposedly occur at a
704 higher oxidative level, not yet attained during the experiments.
705
706 ## 4.3 Alteration progress
707 Assuming that H_2 is entirely produced by arfvedsonite dissolution through oxidation
708 of structural Fe^{II} into Fe^{III}, one can calculate the extent of alteration progress. Given i) the
709 molar mass of arfvedsonite (~960 g mol^{-1}), ii) the Fe^{II} stoichiometry in arfvedsonite (3.07
710 mole Fe(II) per mole of arfvedsonite), and iii) the mass balanced H_2 production from Fe^{II}

oxidation into Fe^{III} (the generalized reaction can be represented according to the **Equation 2**), we estimate that 1 kg of arfvedsonite can produce a maximum of 1.54 moles of H_2 if all the Fe^{II} is oxidized into Fe^{III}.

$$2Fe^{II}O + H_2O = Fe_2^{III}O_3 + H_2 \qquad (2)$$

Note that using the **Equation 1** to calculate the H_2 production from arfvedsonite oxidation leads to a similar result: 1.74 moles of H_2 produced per kg of arfvedsonite reacted. For comparison, McCollom et al. (2016) show that complete serpentinization of 1 kg San Carlos olivine produces up to 0.3 moles of H_2 at 265–300 °C. Thus, arfvedsonite alteration can produce ~5 times more H_2 than olivine serpentinization, per mass unit of mineral reacted. Similarly, the H_2 production from SL-Granite and peridotite can also be compared. The latter can produce about 0.37 moles of H_2 per kg of rock altered, assuming an FeO content of 8 wt% and that 66% of the iron gets oxidized during serpentinization (Klein et al., 2014). Because arfvedsonite represents only 10 wt% of SL-granite, the H_2 potential of this rock is 0.17 moles per kg, which is about two times less than that of peridotite.

Using these mass balance calculations, together with the known amounts of H_2 produced during the experiments, allows estimating the minimum amount of arfvedsonite reacted. It turns out that at least 23 wt% of arfvedsonite were dissolved in the experiment where SL-granite was reacted at 350–400 °C, in an initial pure water medium. Similarly, ~8 wt% arfvedsonite was dissolved during run #SL1 where SL-granite was reacted at 280 °C in the presence of pure water. Given the proportions of arfvedsonite in SL-granite (10 wt%), these maximum estimates are in line with SEM and XRD observations made on the reacted solid reaction products. In the case of experiments conducted with pure arfvedsonite at 350 °C with either pure water, or water + 3 m NaCl + 0.1 m NaOH, our estimate implies that ~10 wt% arfvedsonite would have reacted. This value contrasts with the rather weak dissolution/precipitation features observed at the surface of arfvedsonite after these two

736 experiments, and the non-detection of secondary by-products by XRD analysis. To account
737 for the latter, one explanation may lie in the low water-to-rock mass ratio (W/R = 1) in these
738 experiments. Another possibility is that secondary phases were lost during the opening of the
739 gold capsule, as its strong deformation and the low mass of reacted material render this
740 operation quite complex. More experiments using longer reaction time and higher amounts of
741 sample will help shedding more light on the mechanism of arfvedsonite alteration.

742

743 ### 4.4. Rate of H_2 generation and comparison with serpentinization

744 Hydrogen production recorded as a function of time during our hydrothermal
745 experiment carried out at 280 °C (#SL1) and 350 °C in the presence of a sieved fraction of
746 SL-granite (53 – 212 μm) can be compared with experiments carried out at 300 °C on
747 harzburgite and San Carlos olivine powder of similar grain size by Grozeva et al. (2017) and
748 McCollom et al. (2016), respectively (**Fig. 9**). The water/rock ratio is the main significant
749 parameter that differs from these experiments. Hydrogen concentration data from Grozeva et
750 al. (2017) have been recomputed to be plotted in the same unit as the other experiments (i.e
751 mmol of H_2 per kg of rock – see **Supplementary Table S3**). Hydrogen generation rates from
752 SL-granite and harzburgite alteration are similar, at least during the early stage of reaction.
753 After 500 hours of reaction time, the total amount of H_2 generated during run #SL1 was 1.5
754 times greater than that obtained with San Carlos olivine.

755 In our run, after 48 hours at 280 °C, H_2 was generated at a relatively constant rate of
756 1.47×10^{-5} mol kg_{rock}^{-1} h^{-1}. Assuming that all H_2 is produced from arfvedsonite alteration (10
757 wt% of granite), and given the specific surface area of this amphibole (0.30 m^2 g^{-1}), we obtain
758 a rate of H_2 production of about 1100 pmol cm^{-2} day^{-1}. This value lies within the range of H_2
759 production rate reported for olivine serpentinization by McCollom et al. (2016) at 300 °C: 100
760 – 2000 pmol cm^{-2} day^{-1}. The rate of hydrogen production derived from the experiment carried

761 out at 350 – 400 °C and 400 bar (#SL9) is about 2 times higher than at 280 °C: 3.0×10^{-5} mol
762 kg_{rock}^{-1} h^{-1} or 2200 $pmol.cm^{-2}.day^{-1}$. The absence of coating or passivation observed at the
763 surface of the arfvedsonite clearly plays in favor of a high rate of alteration, as no diffusion
764 process of the reactants through secondary phases is there to slow the reaction down. During
765 olivine serpentinization, hydrogen production rate peaks at about 300 °C and then decreases
766 abruptly as temperature increases. This is because olivine, being part of the equilibrium
767 mineral assemblage, limits the amount of Fe(II) available for H_2 generation (McCollom et al.,
768 2016). Currently, the temperature dependence of H_2 production rate during arfvedsonite
769 alteration is poorly constrained, but the trend observed for olivine serpentinization does not
770 seem to be valid for peralkaline granite.

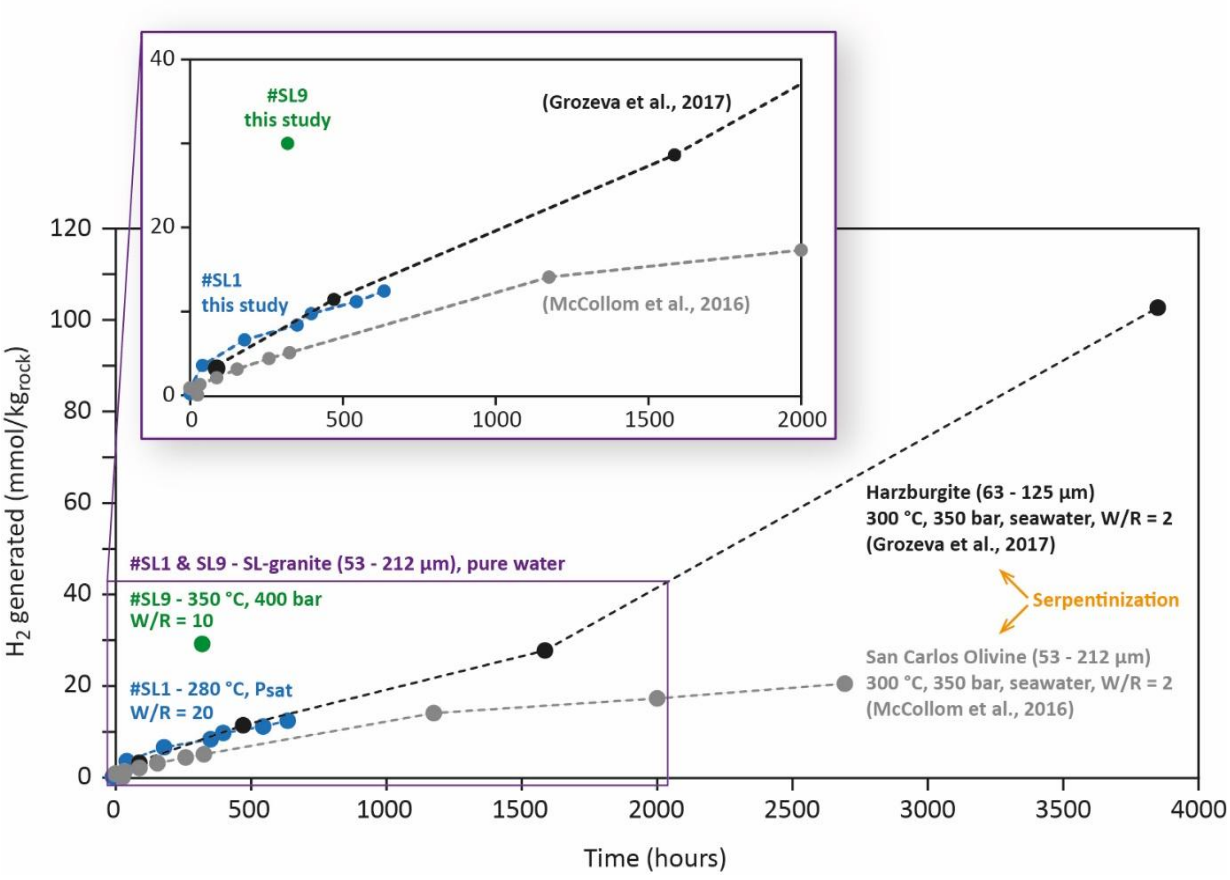

771
772

773 **Figure 9.** Comparison of H_2 generation during San Carlos olivine (grey dots), and harzburgite
774 (black dots) serpentinization at 300 °C, with SL granite hydrothermal alteration at 280 °C (red
775 dots) and 350 °C (green dot). The inset graph is a zoom on the first 2000 hours of reaction.

However, it seems clear that the presence of the minerals forming the granite has a strong impact on the H_2 production rate, as mentioned previously. In particular, albite and microcline are an important source of aluminum, an element that plays a key role in the precipitation of phyllosilicates. As already observed for serpentinization (Andreani et al., 2013), presence of aluminum may increase both the solubility and dissolution rate of arfvedsonite, by enhancing the precipitation of phyllosilicates such as chlorite and montmorillonite.

4.5 Implications for H_2 production and exploration in peralkaline rocks

If there is a consensus in the scientific community on the abiotic origin of hydrogen, methane, and associated higher-order hydrocarbons found in agpaitic peralkaline igneous intrusions, the source of these gases is still subject of debate in the literature (e.g., Marks and Markl, 2017). Some authors consider that CH_4 plus minor to moderate amounts of H_2 exsolve from the magma at 450–500 °C, together with an immiscible aqueous fluid of high salinity (25 wt% NaCl eq.) (Konnerup-Madsen et al., 1985; Beeskow et al., 2006; Krumrei et al. 2007; Vasyukova et al., 2016, 2019). Other workers propose that the hydrocarbons formed by late to post-magmatic Fischer-Tropsch-like synthesis, with the H_2 needed to drive this reaction being produced from alteration of primary igneous minerals such as arfvedsonite (Salvi and Williams-Jones, 1997, Potter et al., 2004; 2013). Production of some H_2 by polymerization of primary hydrocarbons has also been proposed (Krumrei et al. 2007).

At Strange Lake, early CH_4-rich inclusions may contain up to 97 mol% CH_4 and 3 mol% H_2 (Salvi and Williams-Jones, 1992, 1997, 2006; Vasyukova et al., 2016). From the spatial distribution of fluid and melt inclusions, Vasyukova et al. (2016) inferred that the fluid carrying these reduced gases coexisted with a pegmatite melt at the time of entrapment and

concluded that it had exsolved from the melt. However, the fate of H_2 remains unclear, as this molecule was also measured in secondary fluid inclusions by the same authors. Also, most of the fluid inclusion data collected so far at Strange Lake rely on bulk gas analysis (Salvi and Williams-Jones, 1997; Vasyukova et al., 2016), and the few in-situ Raman measurements available (Vasyukova et al., 2016) were not designed to specifically target H_2 – as these authors point out, its strongest vibration at 4156 cm^{-1} is beyond the wavenumbers range accessible with the spectrometer used. On the other hand, Potter et al. (2004) were able to measure up to 40 mol% H_2 at 400 bar in CH_4-dominant fluid inclusions from the Lovozero pluton (Kola Peninsula, Russia), using a mass spectrometer coupled to an on-line GC-crusher system (see also Salvi and Williams-Jones, 2003). Based on detailed fluid inclusion petrography, in situ Raman spectroscopy and textural relationships, Potter and coworkers concluded that these inclusions were trapped during post-magmatic hydrothermal alteration of an early mineral assemblage. The rarity of H_2O-dominant inclusions in the Lovozero samples and the coexistence of these inclusions in the same trails as the CH_4-dominant inclusions implies coeval, immiscible trapping of the aqueous and the carbonic fluids, at or below the CH_4 - H_2O solvus at ~350 °C, leaning towards a post-magmatic origin. This is also supported by the microthermometric data for the H_2O-dominant inclusions, which homogenize to vapor between 290 and 350 °C.

The data presented here do not resolve this debate, but they clearly demonstrate that H_2 can be produced by water-rock interaction, i.e., during the post-magmatic stage, via the alteration of arfvedsonite to aegirine, a widespread process in peralkaline rocks, particularly the agpaitic variety (e.g., Bernard et al., 2020). Given the depth of these plutons (maximum of 12.5 km for the Khibiny and Lovozero system; Arzamastsev et al., 2000, 2013), it is possible that, in some cases, temperatures of ca. 200 °C or above may sustain active hydrothermal activity that could produce alteration of these rocks at depth, thereby triggering H_2 generation,

826 nowadays. Agpaitic peralkaline igneous intrusion may thus represent fertile geological setting
827 for H_2 exploration for energy production purposes.
828
829 ## 5. Conclusion
830 The results of this study clearly show that H_2 can be produced via the hydrothermal
831 alteration of arfvedsonite at $T \geq 280$ °C in agpaitic peralkaline igneous intrusions. Oxidation
832 of structural Fe^{II} into Fe^{III} with concomitant reduction of water explains well this observation.
833 After experimental reaction, arfvedsonite exhibits obvious dissolution feature at its surface,
834 and magnetite, phyllosilicates and secondary zircons become present. Circumneutral to
835 alkaline conditions clearly promote H_2 generation as it is the case for serpentinization.
836 Hydrogen generation is also enhanced when reacting granite instead of only arfvedsonite.
837 Aluminum, from alkali feldspar dissolution, may increase the solubility of arfvedsonite
838 through the precipitation of phyllosilicates. In terms of rate, H_2 generation from arfvedsonite
839 alteration in the presence of granite is a more efficient process than serpentinization of olivine
840 or harzburgite.

841 Aegirine, a very common product of arfvedsonite alteration in these granites, was not
842 observed in this study. The effect of pressure, oxygen fugacity, and length of reaction time
843 remains to be evaluated to better constrain the reaction kinetics. Vasyukova et al. (2016)
844 propose that the cooling of Strange Lake pluton was isobaric and, based on the intersection of
845 isochores for carbonic and aqueous fluid inclusions, took place at a pressure of ~1100 bar.
846 They also note that late alteration of arfvedsonite may continue at temperature as low as 150
847 °C, with hematite and Fe-celadonite as secondary alteration phases (Vasyukova and
848 Williams-Jones, 2019). Thus, alteration of arfvedsonite and SL-granite at lower temperature
849 would also deserve further investigations.

Acknowledgments

This study was financially supported by CNRS -INSU (project CESSUR) and the French National Research Agency ANR through the H2Kola project (AAPG 2020 – CE01 – H2KOLA). Laurent Truche acknowledges support from the Institut Universitaire de France. Gilles Bessaque is warmly thanked for his constant help while handling the Coretest autoclave and fixing numerous leakage and seizing issues. EPMA and XRD analysis were carried out at ISTerre by Valentina Batanova and Nathaniel Findling, respectively. We are most grateful to the PSI SLS synchrotron, especially Benjamin Watts (PolLux beamline) for technical advice, and to the SOLEIL synchrotron, especially Rachid Belkhou for user support. Thanks are also extended to David Troadec and IEMN (Cité Scientifique, av. Poincaré CS 60069, 59652 Villeneuve d'Ascq Cedex). The TEM national facility at Institut Chevreul (Lille, France) is supported by the Conseil Régional du Nord-Pas de Calais, the European Regional Development Fund (ERDF), and the Institut National des Sciences de l'Univers (INSU, CNRS).

Figure captions

Figure 1. Geological map of the Strange Lake pluton (courtesy of O. Vasyukova) locating the sample of hypersolvus granite used for the experiments (left-hand side). On the right-hand side is shown a sample of altered pegmatite where the replacement of arfvedsonite (large dark green crystals) by aegirine (light green) is clearly visible. The fluid inclusions displayed in the inset represent an example of coexisting L- and V-rich populations, where the latter inclusions

contain hydrogen as well as higher-order hydrocarbons, showing fluorescence under UV illumination. qtz = quartz, fds = feldspars, arf = arfvedsonite, aeg = aegirine.

Figure 2. Production of H_2 after 360 hours elapsed time in the gold capsule experiments carried out at 350 °C and 500 bar. Different initial fluid compositions were tested to evaluate the effect of pH and salinity. (a) Experiments carried out in the presence of SL-granite (red) or arfvedsonite (black) are compared to the blanks: fluid only (dashed lines) or quartz + 3 m NaCl (grey star). The notation "dry" indicates that the gold capsule was loaded with solid material only (no fluid). The 2 replicates performed in the presence of water + SL-granite or arfvedsonite are shown in light red and light grey, respectively. (b) Production of H_2 normalized to the mass of solids (SL-granite or arfvedsonite) as a function of fluid composition. Error bars reflect the cumulative uncertainty associated with measuring the volume of gas released after piercing the gold capsules and with the analytical uncertainty.

Figure 3. Production of CH_4 and CO_2 after 360 hours elapsed time in gold capsule experiments carried out at 350 °C and 500 bar. (a) and (b) moles of CO_2 and CH_4 produced in the gold capsules as a function of fluid composition, respectively. The annotation "dry" indicates that the gold capsule was loaded with solid material only (no fluid). (c) and (d) show production of CO_2 and CH_4 normalized to the mass of solids (SL-granite or arfvedsonite) as a function of fluid composition, respectively. The orange dashed line depicts a trend of decreasing CO_2 concomitant with increasing pH of the fluid.

Figure 4. Production of H_2 (blue diamonds) and CO_2 (red squares) as a function of time during experiment #SL1 carried out at 280 °C, 70 bar (Psat + Ar) in the presence of water and SL-granite. Error bars are smaller than the size of the symbols.

898

899 **Figure 5.** Production of H_2 (blue diamonds), CO_2 (red squares) and CH_4 (green triangles) as a
900 function of time during experiment #SL9 carried out in the presence of water and SL-granite.
901 Temperature, pressure and fluid composition evolve according to 3 consecutive steps as
902 indicated on the figure: 1) 350 °C, 400 bar, pure water initially, then 2) a temperature increase
903 to 400 °C at constant pressure 400 bar, and finally 3) NaCl injection and pressure decrease to
904 260 bar at 400 °C. This last step induced phase separation to produce coexisting brine
905 (density = 0.70 g cm^{-1}, 2.7 m NaCl) and vapor (density = 0.19 g cm^{-1}, 0.028 m NaCl). During
906 this stage, sampling was performed from the vapor phase. Error bars are smaller than the size
907 of the symbols.

908

909 **Figure 6.** Back-scattered electron (BSE) and secondary electron (SE) images of unreacted
910 arfvedsonite and representative reaction products after hydrothermal alteration of SL-granite
911 at 280, 350 and 400 °C. (a) BSE image of unreacted arfvedsonite (Arfv). (b) BSE image of
912 arfvedsonite after reaction at 280 °C (run #SL1) with tiny isolated zircon lumps (<200 nm) on
913 its surface (inset). (c) BSE image of Fe-rich phyllosilicate (Fe-Phyllo) observed in the bulk
914 solids after hydrothermal alteration of SL-granite at 280 °C (run #SL1). (d) BSE images of
915 magnetite (Mgt) crystals imbedded in mats of platy Fe-phyllosilicate after reaction at 280 °C
916 (run #SL1). Quartz (Qtz) and K-feldspar (K-Feld) crystals from SL-granite are also visible.
917 (e) and (f) SE images of arfvedsonite after hydrothermal alteration of SL-granite at 350 °C in
918 the presence of water. The surface of arfvedsonite displays clear dissolution features on the
919 edges, corners and cleavage surfaces (red arrows). The inset in (e) shows the presence of tiny
920 fibrous precipitates along the arfvedsonite cleavages. The surface of arfvedsonite in (f) is also
921 covered with tiny isolated zircon lumps. (g) BSE image of arfvedsonite crystals nearly fully
922 coated by octahedral interbedded magnetite (Mgt) crystals after reaction at 400 °C (run

#SL9). (h) BSE image of arfvedsonite crystals fully coated by magnetite and phyllosilicates after reaction at 400 °C (run #SL9).

Figure 7. SEM and TEM images of arfvedsonite-zircon nodule interface. (a) SEM image of carbon-coated arfvedsonite crystal covered with nanometric nodules. (b) SEM image of the crystal area targeted for FIB foil cutting. The emplacement of the FIB foil is identified by a platinum deposit (in the shape of a cross and dots). (c) FIB foil extracted from the section defined in (b), with a continuous platinum strap on top of it. The FIB foil presents different cutting thicknesses, the arfvedsonite-zircon nodule interface being the thinnest area. Carbon coating is also visible. (d) Bright-field TEM image of the FIB foil from (c) showing radial-growth of zircon nodules placed on the clean surface of the arfvedsonite crystal. Platinum strap (Pt) and carbon coating are indicated. (e) Expanded view from image (d) presenting a polycrystalline zircon nodule in contact with arfvedsonite. (f) High-resolution TEM image of the interface, showing the crystalline structure of the two phases, with no inter-crystalline connection.

Figure 8. Representative XANES spectra at the Fe $L_{2,3}$-edges for unreacted (in red) and reacted (#SL1 in blue, #SL9 in green) arfvedsonites. Spectra have been normalized to the integral Fe L_3-edge intensity, and shifted vertically for clarity (normalised intensity with arbitrary unit). The vertical dashed lines represent the energies fixed to determine the Fe^{3+}/Fe_{total} ratio from the intensities of L_3-peaks, according to the procedure of Bourdelle et al. (2013).

Figure 9. Comparison of H_2 generation during San Carlos olivine (grey dots), and harzburgite (black dots) serpentinization at 300 °C, with SL granite hydrothermal alteration at 280 °C (red dots) and 350 °C (green dot). The inset graph is a zoom on the first 2000 hours of reaction.

References

Arzamastsev, A.A., Glaznev, V.N., Raevsky, A.B. and Arzamastseva, L.V., 2000. Morphology and internal structure of the Kola Alkaline intrusions, NE Fennoscandian Shield: 3D density modelling and geological implications. Journal of Asian Earth Sciences, 18(2), pp.213-228.

Arzamastsev, A.A., Arzamastseva, L.V., Zhirova, A.M. and Glaznev, V.N., 2013. Model of formation of the Khibiny-Lovozero ore-bearing volcanic-plutonic complex. Geology of Ore Deposits, 55(5), pp.341-356.

Andreani, M., Daniel, I. and Pollet-Villard, M., 2013. Aluminum speeds up the hydrothermal alteration of olivine. American Mineralogist, 98(10), pp.1738-1744.

Bazarkina, E.F., Chou, I.M., Goncharov, A.F. and Akinfiev, N.N., 2020. The Behavior of H_2 in Aqueous Fluids under High Temperature and Pressure. Elements: An International Magazine of Mineralogy, Geochemistry, and Petrology, 16(1), pp.33-38.

Beeskow, B., Treloar, P.J., Rankin, A.H., Vennemann, T.W. and Spangenberg, J., 2006. A reassessment of models for hydrocarbon generation in the Khibiny nepheline syenite complex, Kola Peninsula, Russia. Lithos, 91(1-4), pp.1-18

971

972 Belkhou, Rachid, Stefan Stanescu, Sufal Swaraj, Adrien Besson, Milena Ledoux, Mahdi
973 Hajlaoui, and Didier Dalle. 2015. 'HERMES: A Soft X-Ray Beamline Dedicated to X-Ray
974 Microscopy'. Journal of Synchrotron Radiation 22 (4): 968–79.

975

976 Bernard, C., Estrade, G., Salvi, S., Béziat, D. and Smith, M., 2020. Alkali pyroxenes and
977 amphiboles: a window on rare earth elements and other high field strength elements behavior
978 through the magmatic-hydrothermal transition of peralkaline granitic systems. Contributions
979 to Mineralogy and Petrology, 175(9), pp.1-27.

980

981 Boreham, C.J., Sohn, J.H., Cox, N., Williams, J., Hong, Z. and Kendrick, M.A., 2021.
982 Hydrogen and hydrocarbons associated with the Neoarchean Frog's Leg Gold Camp, Yilgarn
983 Craton, Western Australia. *Chemical Geology*, p.120098.

984

985 Bourdelle, Franck, Karim Benzerara, Olivier Beyssac, Julie Cosmidis, Daniel R. Neuville,
986 Gordon E. Brown, and Erwan Paineau. 2013. 'Quantification of the Ferric/Ferrous Iron Ratio
987 in Silicates by Scanning Transmission X-Ray Microscopy at the Fe L-2,L-3 Edges'.
988 Contributions to Mineralogy and Petrology 166 (2): 423–34.

989

990 Bourdelle, Franck, Teddy Parra, Olivier Beyssac, Christian Chopin, and Florent Moreau.
991 2012. 'Ultrathin Section Preparation of Phyllosilicates by Focused Ion Beam Milling for
992 Quantitative Analysis by TEM-EDX'. Applied Clay Science 59–60 (May): 121–30.

993

994 Chavagnac, V., Monnin, C., Ceuleneer, G., Boulart, C. and Hoareau, G., 2013.
995 Characterization of hyperalkaline fluids produced by low-temperature serpentinization of

mantle peridotites in the Oman and Ligurian ophiolites. Geochemistry, Geophysics, Geosystems, 14(7), pp.2496-2522.

Cannat, M., Fontaine, F. and Escartin, J., 2010. Serpentinization and associated hydrogen and methane fluxes at slow spreading ridges. In *Diversity of Hydrothermal Systems on Slow Spreading Ocean Ridges*; Rona, P.A., Devey, C.W., Dyment, J., Murton, B.J., Eds.; AGU Geophysical Monograph Series; John Wiley and Sons: Hoboken, NJ, USA, 2010; Volume 188.

Charlou, J.L., Donval, J.P., Fouquet, Y., Jean-Baptiste, P. and Holm, N., 2002. Geochemistry of high H_2 and CH_4 vent fluids issuing from ultramafic rocks at the Rainbow hydrothermal field (36 14′ N, MAR). Chemical geology, 191(4), pp.345-359.

Chou, I.M., 1986. Permeability of precious metals to hydrogen at 2kb total pressure and elevated temperatures. American Journal of Science, 286(8), pp.638-658.

Coveney Jr, R.M., Goebel, E.D., Zeller, E.J., Dreschhoff, G.A. and Angino, E.E., 1987. Serpentinization and the origin of hydrogen gas in Kansas. AAPG Bulletin, 71(1), pp.39-48.

Decarreau A., Petit S., Vieillard P. and Dabert N., 2004. Hydrothermal synthesis of aegirine at 200 °C. Eur. J. Mineral., 16, pp.85–90.

Donzé, F.V., Truche, L., Shekari Namin, P., Lefeuvre, N. and Bazarkina, E.F., 2020. Migration of natural hydrogen from deep-seated sources in the São Francisco Basin, Brazil. Geosciences, *10*, p.346.

Drobner, E., Huber, H., Wächtershäuser, G., Rose, D. and Stetter, K.O., 1990. Pyrite formation linked with hydrogen evolution under anaerobic conditions. Nature, 346(6286), pp.742-744.

Fernandez-Prini, R., Alvarez, J.L. and Harvey, A.H., 2004. Aqueous solubility of volatile nonelectrolytes. In Aqueous Systems at Elevated Temperatures and Pressures (pp. 73-98). Academic Press.

Gaucher, E.C., 2020. New Perspectives in the Industrial Exploration for Native Hydrogen. Elements: An International Magazine of Mineralogy, Geochemistry, and Petrology, 16(1), pp.8-9.

Grozeva, N.G., Klein, F., Seewald, J.S. and Sylva, S.P., 2017. Experimental study of carbonate formation in oceanic peridotite. Geochimica et Cosmochimica Acta, 199, pp.264-286.

Gysi, A.P. and Williams-Jones, A.E., 2013. Hydrothermal mobilization of pegmatite-hosted REE and Zr at Strange Lake, Canada: A reaction path model. Geochimica et Cosmochimica Acta, 122, pp.324-352.

Gysi, A.P., Williams-Jones, A.E. and Collins, P., 2016. Lithogeochemical vectors for hydrothermal processes in the Strange Lake peralkaline granitic REE-Zr-Nb deposit. Economic Geology, 111(5), pp.1241-1276.

Hirose, T., Kawagucci, S. and Suzuki, K., 2011. Mechanoradical H2 generation during simulated faulting: Implications for an earthquake-driven subsurface biosphere. Geophysical research letters, 38(17).

Hitchcock, Adam P. 2012. 'Soft X-Ray Imaging and Spectromicroscopy'. In Handbook of Nanoscopy, edited by Gustaaf Van Tendeloo, Dirk Van Dyck, and Stephen J. Pennycook, 745–91. Weinheim, Germany: Wiley-VCH Verlag GmbH & Co. KGaA.

Ikorskiy, S.V., 1986. Methods of examining the compositions of gases in closed microjoints in Khibiny-intrusion rocks. Geochem. Int. 7, 70–74

Jarosewich, E. J., Nelen, J. A. & Norberg, J. A. (1980). Reference samples for electron microprobe analysis. Geostandards Newsletter 4, 4347

Klein, F., Bach, W. and McCollom, T.M., 2013. Compositional controls on hydrogen generation during serpentinization of ultramafic rocks. Lithos, 178, pp.55-69.

Klein, F., Bach, W., Humphris, S.E., Kahl, W.A., Jöns, N., Moskowitz, B. and Berquó, T.S., 2014. Magnetite in seafloor serpentinite—Some like it hot. Geology, 42(2), pp.135-138.

Klein, F., Grozeva, N.G., Seewald, J.S., McCollom, T.M., Humphris, S.E., Moskowitz, B., Berquó, T.S. and Kahl, W.A., 2015. Experimental constraints on fluid-rock reactions during incipient serpentinization of harzburgite. American Mineralogist, 100(4), pp.991-1002.

Klein, F., Tarnas, J.D. and Bach, W., 2020. Abiotic sources of molecular hydrogen on Earth. Elements: An International Magazine of Mineralogy, Geochemistry, and Petrology, 16(1), pp.19-24.

Konnerup-Madsen, J., Dubessy, J., Rose-Hansen, J., 1985. Combined Raman microprobe spectrometry and microthermometry of fluid inclusions in minerals from igneous rocks of the Gardar Province (South Greenland). Lithos 18, 271–280.

Konnerup-Madsen, J., 2001. A review of the composition and evolution of hydrocarbon gases during solidification of the Ilímaussaq complex, South Greenland. Geol. Greenl. Surv. Bull. 190, 163–170.

Krumrei, T.V., Pernicka, E., Kaliwoda, M., Markl, G., 2007. Volatiles in a peralkaline system: Abiogenic hydrocarbons and F–Cl–Br systematics in the naujaite of the Ilímaussaq intrusion, South Greenland. Lithos 95, 298–314.

Lamadrid, H.M., Rimstidt, J.D., Schwarzenbach, E.M., Klein, F., Ulrich, S., Dolocan, A. and Bodnar, R.J., 2017. Effect of water activity on rates of serpentinization of olivine. Nature communications, 8(1), pp.1-9.

Li, X., Zhang, C., Behrens, H., and Holtz, F., 2020. Calculating amphibole formula from electron microprobe analysis data using a machine learning method based on principal components regression. Lithos, 105469.

Lin, L.H., Slater, G.F., Sherwood-Lollar, B.S., Lacrampe-Couloume, G. and Onstott, T.C., 2005. The yield and isotopic composition of radiolytic H_2, a potential energy source for the deep subsurface biosphere. Geochimica et Cosmochimica Acta, 69(4), pp.893-903.

Malvoisin, B., Brunet, F., Carlut, J., Montes-Hernandez, G., Findling, N., Lanson, M., Vidal, O., Bottero, J.Y. and Goffé, B., 2013. High-purity hydrogen gas from the reaction between BOF steel slag and water in the 473–673 K range. International journal of hydrogen energy, 38(18), pp.7382-7393.

Marks, M.A.W., Markl, G., 2017. A global review on agpaitic rocks. Earth-Sci. Rev. 173, 229–258.

McCollom, T.M., Klein, F., Robbins, M., Moskowitz, B., Berquó, T.S., Jöns, N., Bach, W. and Templeton, A., 2016. Temperature trends for reaction rates, hydrogen generation, and partitioning of iron during experimental serpentinization of olivine. Geochimica et Cosmochimica Acta, 181, pp.175-200.

McCollom, T.M., Klein, F., Moskowitz, B., Berquó, T.S., Bach, W. and Templeton, A.S., 2020a. Hydrogen Generation and Iron Partitioning During Experimental Serpentinization of an Olivine–Pyroxene Mixture. Geochimica et Cosmochimica Acta, 282, pp. 55-75.

McCollom, T.M., Klein, F., Solheid, P. and Moskowitz, B., 2020b. The effect of pH on rates of reaction and hydrogen generation during serpentinization. Philosophical Transactions of the Royal Society A, 378(2165), p.20180428.

Ménez, B., 2020. Abiotic hydrogen and methane: Fuels for life. Elements: An International Magazine of Mineralogy, Geochemistry, and Petrology, 16(1), pp.39-46.

Milesi, V., Guyot, F., Brunet, F., Richard, L., Recham, N., Benedetti, M., Dairou, J. and Prinzhofer, A., 2015. Formation of CO_2, H_2 and condensed carbon from siderite dissolution in the 200–300 C range and at 50 MPa. Geochimica et Cosmochimica Acta, 154, pp.201-211.

Murray, J., Clément, A., Fritz, B., Schmittbuhl, J., Bordmann, V. and Fleury, J.M., 2020. Abiotic hydrogen generation from biotite-rich granite: A case study of the Soultz-sous-Forêts geothermal site, France. Applied Geochemistry, p.104631.

Neal, C. and Stanger, G., 1983. Hydrogen generation from mantle source rocks in Oman. Earth and Planetary Science Letters, 66, pp.315-320.

Nivin, V.A., Devirts, A.L., Lagutina, Y.P., 1995. The origin of the gas phase in the Lovozero massif based on hydrogen-isotope data. Geochem. Int. 32, 65–71.

Nivin, V.A., Belov, N.I., Treloar, P.J., Timofeyev, V.V., 2001. Relationship between gas geochemistry and release rates and the stressed state of igneous rock massifs. Tectonophysics 336, 233–244.

Nivin, V.A., 2016. Free hydrogen-hydrocarbon gases from the Lovozero loparite deposit (Kola Peninsula, NW Russia). Applied Geochemistry, 74, pp.44-55.

Nivin, V.A., 2019. Occurrence forms, composition, distribution, origin and potential hazard of natural hydrogen–hydrocarbon gases in ore deposits of the Khibiny and Lovozero Massifs: a review. Minerals, 9(9), p.535.

Nivin, V., 2020. The Origin of Hydrocarbon Gases in the Lovozero Nepheline-Syenite Massif (Kola Peninsula, NW Russia), as Revealed from He and Ar Isotope Evidence. Minerals, 10(9), p.830.

Potter, J., Konnerup-Madsen, J., 2003. A review of the occurrence and origin of abiogenic hydrocarbons in igneous rocks. In: Petford, N., McCaffrey, K.J.W. (Eds.), Hydrocarbons in Crystalline Rocks. Geol. Soc. Lon. Spec. Pub., vol. 214, pp. 151–173.

Potter, J., Rankin, A.H. and Treloar, P.J., 2004. Abiogenic Fischer–Tropsch synthesis of hydrocarbons in alkaline igneous rocks; fluid inclusion, textural and isotopic evidence from the Lovozero complex, NW Russia. Lithos, *75*(3-4), pp.311-330.

Potter, J., Salvi, S. and Longstaffe, F.J., 2013. Abiogenic hydrocarbon isotopic signatures in granitic rocks: Identifying pathways of formation. Lithos, 182, pp.114-124.

Raabe, J., G. Tzvetkov, U. Flechsig, M. Boege, A. Jaggi, B. Sarafimov, M. G. C. Vernooij, et al., 2008. 'PolLux: A New Facility for Soft X-Ray Spectromicroscopy at the Swiss Light Source'. Review of Scientific Instruments 79 (11): 113704. https://doi.org/10.1063/1.3021472.

Salvi, S., Williams-Jones, A.E., 1992. Reduced orthomagmatic C–O–H–N–NaCl fluids in the Strange Lake rare-metal granitic complex, Quebec/Labrador, Canada. European Journal of Mineralogy 4, 1155–1174.

Salvi, S., Williams-Jones, A.E., 1997. Fischer–Tropsch synthesis of hydrocarbons during sub-solidus alteration of the Strange Lake peralkaline granite, Quebec/Labrador, Canada. Geochim. Cosmochim. Acta 61, 83–99.

Salvi, S., Williams-Jones, A.E., 2003. Bulk analysis of volatiles in fluid inclusions. In: Samson, I.M., Anderson, A., Marshall, D. (Eds.), Fluid Inclusions: Analysis and Interpretation, Mineralogical Association of Canada, Short Course, vol. 32, pp. 247–278.

Salvi, S., Williams-Jones, A.E., 2006. Alteration, HFSE mineralisation and hydrocarbon formation in peralkaline systems: Insights from the Strange Lake Pluton, Canada. Lithos 91, 19–34.

Seward, T.M. and Franck, E.U., 1981. The system hydrogen-water up to 440° C and 2500 bar pressure. Berichte der Bunsengesellschaft für physikalische Chemie, 85(1), pp.2-7.

Sherwood Lollar, B., Onstott, T., Lacrampe-Couloume, G. and Ballentine, C.J., 2014. The contribution of the Precambrian continental lithosphere to global H_2 production. Nature 516, 379–382.

Shvarov, Y.V., 2008. HCh: new potentialities for the thermodynamic simulation of geochemical systems offered by Windows. Geochem. Int. 46, 834–839.

Siegel, K., Vasyukova, O.V. and Williams-Jones, A.E., 2018. Magmatic evolution and controls on rare metal-enrichment of the Strange Lake A-type peralkaline granitic pluton, Québec-Labrador. Lithos, 308, pp.34-52.

Sleep, N.H., Meibom, A., Fridriksson, Th., Coleman, R.G., and Bird, D.K., 2004. H_2-rich fluids from serpentinization: geochemical and biotic implications. Proc Natl Acad Sci USA 101, 12818–12823.

Smith, N.J.P., Shepherd, T.J., Styles, M.T. and Williams, G.M., 2005, January. Hydrogen exploration: a review of global hydrogen accumulations and implications for prospective areas in NW Europe. In Geological Society, London, Petroleum Geology Conference series (Vol. 6, No. 1, pp. 349-358). Geological Society of London.

Stefánsson, A. and Seward, T.M., 2003. Stability of chloridogold (I) complexes in aqueous solutions from 300 to 600 C and from 500 to 1800 bar. Geochimica et Cosmochimica Acta, 67(23), pp.4559-4576.

Prinzhofer, A., Cissé, C.S.T. and Diallo, A.B., 2018. Discovery of a large accumulation of natural hydrogen in Bourakebougou (Mali). International Journal of Hydrogen Energy, 43(42), pp.19315-19326.

Truche, L., Joubert, G., Dargent, M., Martz, P., Cathelineau, M., Rigaudier, T. and Quirt, D., 2018. Clay minerals trap hydrogen in the Earth's crust: evidence from the Cigar Lake uranium deposit, Athabasca. Earth and Planetary Science Letters, 493, pp.186-197.

Truche, L. and Bazarkina, E.F., 2019. Natural hydrogen the fuel of the 21st century. In E3S Web of Conferences, 98, p. 03006. EDP Sciences.

Truche, L., McCollom, T.M. and Martinez, I., 2020. Hydrogen and Abiotic Hydrocarbons: Molecules that Change the World. Elements: An International Magazine of Mineralogy, Geochemistry, and Petrology, 16(1), pp.13-18.

Vacquand, C., Deville, E., Beaumont, V., Guyot, F., Sissmann, O., Pillot, D., Srcilla, C. and Prinzhofer, A., 2018. Reduced gas seepages in ophiolitic complexes: Evidences for multiple origins of the H_2-CH_4-N_2 gas mixtures. Geochimica et Cosmochimica Acta 223, 437─461. https://doi.org/10.1016/j.gca.2017.12.018

Vasyukova, O.V., Williams-Jones, A.E. and Blamey, N.J.F., 2016. Fluid evolution in the Strange Lake granitic pluton, Canada: Implications for HFSE mobilisation. Chemical Geology, 444, pp.83-100.

Vasyukova, O. V., and A. E. Williams-Jones. "Closed system fluid-mineral-mediated trace element behaviour in peralkaline rare metal pegmatites: Evidence from Strange Lake." Chemical Geology 505 (2019): 86-99.

Worman, S.L., Pratson, L.F., Karson, J.A. and Klein, E.M., 2016. Global rate and distribution of H_2 gas produced by serpentinization within oceanic lithosphere. Geophysical Research Letters, 43(12), pp.6435-6443.

Worman, S.L., Pratson, L.F., Karson, J.A. and Schlesinger, W.H., 2020. Abiotic hydrogen (H_2) sources and sinks near the Mid-Ocean Ridge (MOR) with implications for the subseafloor biosphere. Proceedings of the National Academy of Sciences.